1 **Cryo-electron tomography reveals coupled flavivirus replication, budding and maturation**

2

3 Selma Dahmane[1,2,3,4,5,*,#], Erin Schexnaydre[1,2,3,4,6,*], Jianguo Zhang[1,2,3,4,6,7]*, Ebba Rosendal[3,4,6], Nunya
4 Chotiwan[3,4,6,8], Bina Kumari Singh[1,2,3,4], Wai-Lok Yau[3,4,9,10], Richard Lundmark[3,4,9], Benjamin
5 Barad[11,#], Danielle A. Grotjahn[12], Susanne Liese[13], Andreas Carlson[14], Anna K. Överby[3,4,6#], Lars-
6 Anders Carlson[1,2,3,4,#]

7

8 [1]Department of Medical Biochemistry and Biophysics, Umeå University, Sweden

9 [2]Wallenberg Centre for Molecular Medicine, Umeå University, Sweden

10 [3]The Laboratory for Molecular Infection Medicine Sweden (MIMS), Umeå University, Sweden

11 [4]Umeå Centre for Microbial Research (UCMR), Umeå University, Sweden

12 [5]current address: Friedrich Miescher Institute for Biomedical Research

13 [6]Department of Clinical Microbiology, Umeå University, Sweden

14 [7]current address: Structural Biology, The Rosalind Franklin Institute, United Kingdom

15 [8]current address: Chakri Naruebodindra Medical Institute, Faculty of Medicine Ramathibodi Hospital,
16 Mahidol University, Samut Prakarn 10540, Thailand.

17 [9]Medical and Translational Biology, Umeå University, Sweden

18 [10]current address: Department of Odontology, Umeå University, Sweden

19 [11]Department of Chemical Physiology and Biochemistry, Oregon Health & Science University, USA

20 [12]Department of Integrative Structural and Computational Biology, The Scripps Research Institute,
21 USA

22 [13]Institute of Physics, University of Augsburg, Germany

23 [14]Department of Mathematics, University of Oslo, Norway

24

25 *Equal contribution

26

27 # corresponding authors:

28 selma.dahmane@fmi.ch

29 barad@ohsu.edu

30 anna.overby@umu.se

31 lars-anders.carlson@umu.se

32

33

Abstract

Flaviviruses replicate their genomes in replication organelles (ROs) formed as bud-like invaginations on the endoplasmic reticulum (ER) membrane, which also functions as the site for virion assembly. While this localization is well established, it is not known to what extent viral membrane remodeling, genome replication, virion assembly, and maturation are coordinated. Here, we imaged tick-borne flavivirus replication in human cells using cryo-electron tomography. We find that the RO membrane bud is shaped by a combination of a curvature-establishing coat and the pressure from intraluminal template RNA. A protein complex at the RO base extends to an adjacent membrane, where immature virions bud. Naturally occurring furin site variants determine whether virions mature in the immediate vicinity of ROs. We further visualize replication in mouse brain tissue by cryo-electron tomography. Taken together, these findings reveal a close spatial coupling of flavivirus genome replication, budding, and maturation.

Introduction

Orthoflaviviruses (henceforth flaviviruses) are a large genus of arthropod-borne, positive-sense RNA viruses within the *Flaviviridae* family. The mosquito-borne Dengue virus alone is estimated to yearly cause hundreds of millions of human infections, some progressing to the severe condition known as dengue shock syndrome[1]. Human infections with tick-borne flaviviruses are less frequent, but can have severe outcomes. Tick-borne encephalitis virus (TBEV) is the namesake virus of the "TBEV serocomplex" which includes other tick-borne flaviviruses such as Powassan virus and the low-pathogenic Langat virus (LGTV). Pathogenic tick-borne flaviviruses have a strong neurotropism in mammals, and can cause encephalitis with debilitating or deadly outcome in humans[2].

After entering the cell through endocytosis, the flavivirus genome is translated as a single, transmembrane polyprotein, which is subsequently cleaved by host and viral proteases into ten individual proteins. Seven of these are the non-structural (NS) proteins, which serve to replicate the viral genome. Of the NS proteins, NS3 and NS5 are cytoplasmic enzymes that serve as protease and helicase (NS3), and RNA-dependent RNA polymerase and methyl transferase (NS5). The remaining NS proteins include the endoplasmic reticulum (ER) lumen-resident peripheral membrane protein NS1, and the integral membrane proteins NS2A, NS2B, NS4A and NS4B. Viral genome replication takes place on a transformed, dilated ER containing multiple bud-like membrane invaginations[3,4]. These invaginations, referred to as replication organelles (ROs), are the site of viral RNA replication[5-9]. RO-like membrane rearrangements can be formed by a subset of NS proteins even in the absence of viral RNA replication[5,10,11], but require interactions with host ER proteins[5-9,12,13]. Electron microscopy of resin-embedded, infected cells has shown that the RO is a 80-90 nm, near-spherical bud with a ~10 nm opening towards the cytoplasm[14-17]. However, due to the destruction of protein structure by resin embedding, the organization of proteins and RNA in the RO is still unknown. Virion assembly also takes place at the ER, when a cytoplasmic complex of viral RNA and C protein interacts with the transmembrane envelope proteins prM and E, followed by budding into the ER lumen. NS2A has been suggested as a key viral protein coupling replication and assembly[18-20], and resin-embedding electron microscopy has visualized putative virions in the immediate vicinity of ROs[14,16,21]. Newly formed, immature virions have a spiky surface covered with extended prM-E trimers[22-24]. The cleavage of prM by the host-cell protease furin, which is thought to occur in the trans-Golgi, leads to a structurally rearranged, infectious, mature virion with smoother appearance[25,26]. If virion assembly and maturation are directly linked to ROs is currently unknown.

To shed light on the interactions between flavivirus replication, assembly and maturation, we performed *in situ* cryo-electron tomography[27-31] on human cells and mouse brain tissue infected with LGTV, and a novel, chimeric LGTV carrying TBEV structural proteins. The data suggest a mechanism for RO membrane remodeling, the presence of a protein complex tethering the RO membrane to an apposed ER membrane, and a close proximity of virion assembly and maturation.

Results

Cryo-electron tomography reveals two states of replication organelles in Langat virus-infected cells

To explore the macromolecular architecture of flavivirus ROs, we grew human A549 cells on EM grids and infected them with LGTV. Cells were plunge-frozen at 24 h post infection (h.p.i) and subjected to focused-ion-beam milling, after which lamellas containing the infected cytoplasm were imaged using cryo-electron tomography (cryo-ET) (Table 1). The tomograms revealed a dilated ER inclusive of clustered ROs (Fig. 1 and Supplementary video 1). ROs were clearly identified as near-spherical membrane invaginations into the ER lumen, of a kind not present in uninfected cells (Fig. S1A-B). The vicinity of the remodeled ER contained *bona fide* ribosomes as well as mitochondria immediately apposed to the ER membrane (Fig. 1A-D). ROs frequently appeared in clusters within the lumen of dilated ER, as in Fig. 1A-D in which a single, dilated ER cisterna contained >10 ROs within the field of view (bearing in mind that the RO cluster probably extended beyond the depth of the lamella). The same ER cisterna additionally contained a virus particle with the characteristic spiky appearance of immature flaviviruses (Fig. 1A-B, orange arrow, and Fig. 1D). The majority of ROs contained filamentous densities, presumably the replicating double-stranded form of the viral RNA, within their lumen (Fig. 1A-D). On the other hand, several ROs were devoid of internal filamentous structures (Fig. 1A-C, white arrows). These two types of ROs will henceforth be denoted as 'filled' and 'empty', respectively (Fig. 1E). In 23 tomograms, 83±14% of ROs were filled (Fig. 1F). The empty ROs were significantly smaller with an average diameter of 46±8 nm (N=25), compared to the filled ROs at 85±5 nm (N=63) (Fig. 1G). In summary, we established a workflow to image flavivirus replication by cryo-ET, revealing that ROs exist in two forms: with and without luminal filamentous densities.

A combination of membrane coat and RNA-induced pressure determines RO morphology

ROs of other viruses depend on the pressure from intraluminal double-stranded RNA (dsRNA) to inflate and stabilize the curved RO membrane[32]. The presence of empty LGTV ROs speaks against this mechanism for flaviviruses, and we thus reasoned that a coat might confer a spontaneous curvature to the RO membrane. To investigate whether a curvature-inducing coat is present on ROs, we assessed if RO membrane thickness is in line with a layer of surface-bound protein layer. Indeed, by visual inspection of tomograms, the membranes of both empty and filled ROs appeared thicker than the surrounding ER membrane (Fig. 2A). No distinct, repeating macromolecules were visible on the RO membranes. While this does not exclude the presence of a protein coat composed of smaller or membrane-integral proteins, it does make its characterization by subtomogram averaging less likely to be successful. Instead, we extended our previously developed surface morphometrics toolbox to allow for local estimation of membrane thickness[33]. This software allowes calculation of the average membrane thickness within a user-selected area, based on average density profiles normal to the membrane. Both for single ROs and their surrounding ER membrane, this yielded reliably interpretable density profiles (Fig. 2B-C). Color coding membranes by thickness indicated that RO membranes are consistently thicker than the surrounding ER membrane (Fig. 2D). Indeed, in four tomograms we measured a significant difference in membrane thickness with the ER membrane being 3.4 ± 0.2 nm (N= 4), and RO membranes 4.0 ± 0.2 nm (N =132) (Fig. 2E). On the other hand, the RO membrane thickness appeared largely independent of RO size, as estimated from their radii of curvature (Fig. 2F).

The observation that flavivirus ROs can form without detectable luminal dsRNA, and the consistent presence of a membrane coat, distinguish them from alphavirus ROs that have a near-identical membrane shape. Based on cryo-ET data, we recently published a mathematical model of alphavirus

132   RO membrane budding, which showed that the pressure from intraluminal dsRNA, together with
133   constraint of the membrane neck, is sufficient for the creation of the RO membrane bud[32]. We next
134   adapted this mathematical model to explain flavivirus RO membrane remodeling. We assume that the
135   membrane coat generates a spontaneous curvature H_0 of the RO membrane. Such a spontaneous
136   curvature can be generated by the protein structure as well as by crowding[34]. Furthermore, we consider
137   that in ROs that enclose dsRNA, the RNA exerts a pressure P on the membrane. The total energy E of
138   the RO membrane is then composed of an integral over the membrane surface A and the contribution
139   of the pressure, which scales with the volume V,

140
$$E = \int_A dA[2\kappa(H - H_0)^2 + \sigma] - PV,$$

141   (1)

142   where the first term describes the bending energy according to the Helfrich model, with κ the bending
143   stiffness and H the mean curvature[35]. The second term in Eq. 1 contains the membrane tension σ.
144   Motivated by the experimentally observed shapes, we describe the ROs as spheres with a radius R, as
145   schematically depicted in Fig. 2G, simplifying Eq. (1) to

146
$$E = 8\pi\kappa(1 - H_0 R)^2 + 4\pi\sigma R^2 - \frac{4}{3}\pi P R^3.$$

147   (2)

148   However, there are two unknown factors in Equation (2), the spontaneous curvature H_0 and the
149   pressure P in the RO. Based on our observations above, the membrane coat can be assumed to be
150   comparable for empty and filled ROs. Thus, we can take advantage of the imaging of empty ROs to
151   obtain H_0 at vanishing pressure, $P = 0$. Minimizing Eq. (2) with respect to R, we obtain

152
$$H_0 = \frac{1 + \sqrt{1 - 2\frac{\sigma R^2}{\kappa}}}{2R}$$

153   (3)

154   From the experiments we have obtained an average diameter of the empty ROs to be $2R = 46\ nm$. By
155   using previously estimated parameters[32] for the membrane properties, i.e., $\sigma = 10^{-5} N/m$ and $\kappa = $
156     $10 k_B T$, we predict the spontaneous curvature to be $H_0 = 0.04 nm^{-1}$, which corresponds to a radius of
157   curvature $1/H_0 = 25 nm$. Next, we want to predict the influence of the pressure generated by the RNA
158   on the spherule size. Since the RNA does not affect the spontaneous curvature H_0, we keep the above
159   prediction and minimize Eq. 2 with respect to R, giving

160
$$P = \frac{2(2\kappa H_0^2 R - 2\kappa H_0 + \sigma R)}{R^2}$$

161   (4)

162   Now including the predicted $H_0 = 0.04 nm^{-1}$ with the measured average diameter of RNA-filled ROs
163     $2R = 85\ nm$, we obtain the pressure $P = 5 \cdot 10^{-4}\ k_B T nm^{-3}$. To interpret this value, we compare it
164   with our previous study of alphavirus ROs, which shows that a dsRNA with a length of 2,000-10,000
165   base pairs generates an internal pressure of $10^{-4} - 10^{-3}\ k_B T nm^{-3}$ (see Materials and Methods,
166   section Estimating RO intraluminal pressure).

167   Taken together, flavivirus ROs have a consistently thicker membrane than the surrounding ER,
168   consistent with the presence of small, curvature-stabilizing proteins that set a baseline RO size in the

169 absence of luminal RNA. The size increase from empty to filled ROs is consistent with a single copy
170 of the genome in dsRNA form.

171

Virions form and undergo maturation in the immediate vicinity of replication organelles

173 In our cryo-electron tomograms we consistently observed virions in the vicinity of ROs, underscoring
174 the strong association between replication and virion assembly (Fig. 3A-C). We next wished to use the
175 structure preservation in cryo-ET to study the spatial relation between virion budding and maturation.
176 In the tomograms, virus particles at different stages of maturation were distinguishable: spiky particles
177 corresponding to immature virions as well as smooth, mature virions (Fig. 3A-C). Subtomogram
178 averaging on a small number of virions confirmed the distinct morphology of the immature and
179 mature virions (Fig. 3D-E), and a good match between the *in situ* averages and structures of purified
180 flaviviruses (Fig. S3). The tomograms also included examples of what seemed to be nearly or recently
181 completed virion budding (Fig. 3A-B). In such events, immature virus particles could be observed
182 right at the membrane, across from ROs (Fig. 3A, orange arrow). Both immature and mature virions
183 were consistently found close to ROs, in separate but intertwined membrane compartments (Fig. 3A-
184 C). While immature and mature particles were not observed in the same membrane compartment,
185 seemingly discrete compartments may have been connected beyond the limited thickness of the
186 lamella. To quantitate the relation of immature and mature particles to ROs, we measured the center-
187 center distance of virions to ROs in 5 tomograms. Immature virions were 95±56 nm (N=37), and
188 mature virions 147±41 nm (N=24) from the closest RO (Fig. 3F). The small but significant distance
189 difference (p=0.0003, unpaired t test), together with the observation that immature and mature virions
190 are present in separate compartments, indicates that virion maturation is coupled to a slight spatial
191 separation from ROs but does not necessitate longer-range trafficking. To further investigate the
192 spatial relationship between genome replication, virion assembly and the Golgi apparatus, we
193 performed immunofluorescence light microscopy on fixed, LGTV-infected cells. Furin exhibited co-
194 localization with the Golgi marker GM130 in both uninfected (Fig. S4A-D) and LGTV-infected cells
195 (Fig. 3G-J). Meanwhile, the dsRNA signal was detected in close proximity to and partially
196 overlapping with clusters enriched in furin and GM130 (Fig. 3J). These results corroborate the cryo-
197 ET, reinforcing the close proximity between viral RNA replication, LGTV assembly and maturation
198 within the infected cell. In summary, both virion assembly and maturation can occur in the immediate
199 proximity of ROs, in distinct but intertwined compartments.

200

The TBEV furin site variants R86 and Q86 differ in replication organelle-proximal virion maturation

203 In purified virions, the transition from immature to smooth conformation can be brought about by pH
204 change even in the absence of furin cleavage. Thus, we wanted to test if the observed RO-proximal
205 virion maturation was dependent on the furin site in prM. To do so, we took advantage of our recently
206 characterized chimeric LGTV, which carries the structural proteins prM and E(ectodomain) from
207 TBEV (Fig. 4A). This virus, rLGTV[T:prME], is genetically stable and has a low pathogenicity similar to
208 that of wildtype LGTV[36]. The rLGTV[T:prME] prM and E come from the human TBEV isolate 93/783 of
209 the European subtype, whose prM has an unusual arginine (R) in position 86 where most other strains
210 have a glutamine (Q) (Fig. 4A). This residue is located at the P8 position of the furin cleavage site in
211 prM, and previous studies of flaviviruses has shown that modifications here might influence prM
212 cleavage and virus export[37]. We thus reasoned that R86 may affect furin cleavage efficiency, and
213 provide a naturally occurring tool to study maturation. Hence, we also produced a version of
214 rLGTV[T:prME] with the more common glutamine 86. These chimeric viruses, henceforth referred to as
215 R86 and Q86, only differ in this amino acid residue. Both viruses replicated with similar kinetics in

6

216   A549 cells (Fig. S5A), but the R86 virus had a slightly higher lethality in immunocompromised *Ips1*^{-/-}
217   (IFN-β promoter stimulator 1) mice (5 of 5 mice died with R86, 7 of 10 died with Q86, Fig. 4B). No
218   difference in neurovirulence was detected (Fig. 4C). We next wanted to investigate whether the
219   pathogenicity of R86 as compared to Q86 correlated with different prM cleavage kinetics. In a
220   cleavage assay with a peptide corresponding to residues 81-94 of prM, the R86 sequence was cleaved
221   faster by furin than Q86 (Fig. 4D). We noted that the R86 sequence generates a putative second,
222   minimal recognition site (KR) for other proprotein convertases such as PC1/3 and PC2[38]. In a peptide
223   cleavage assay, the R86 sequence was also cleaved faster than Q86 by PC1/3. However, the cleavage
224   was still completely dependent on the furin recognition site (RTRR), i.e. the putative second PC1/3
225   cleavage site K85-R86 was not sufficient for cleavage by PC1/3 (Fig. 4D). Next, we looked for the
226   presence of unprocessed prM protein in cell supernatant, which would indicate release of immature
227   virus particles. For both viruses, the bulk of cell-bound M was in the form of uncleaved prM, whereas
228   most M in the supernatant was cleaved (Fig. 4E). Interestingly, the R86 chimeric virus had a
229   significantly lower percentage of uncleaved prM in supernatant at 48 h post infection (Fig. 4F),
230   suggesting that R86 confers a more efficient particle maturation. The biochemical and cell assays thus
231   converge on the interpretation that the R86 sequence variant confers faster furin cleavage.

232   Having characterized the different rates of furin cleavage, we then returned to the question of
233   individual virion conformation inside infected cells. We infected cells with R86 and Q86 chimeric
234   viruses and recorded cryo-electron tomograms of the infected cytoplasm as for wildtype LGTV. Both
235   for R86 and Q86, the tomograms showed a similar overall appearance as for wildtype LGTV,
236   including an abundance of filled and empty replication organelles as well as new virions inside dilated
237   ER compartments (Fig. 4G-H, Fig. S5B). In the R86 tomograms, both immature and mature virions
238   were seen, whereas immature virions appeared to predominate in the Q86 tomograms. We calculated
239   the percentage mature virions in a set of tomograms for wildtype LGTV and the chimeric viruses.
240   Whereas the number of virions in individual tomograms was sometimes small, the average fractions
241   mature particles over several tomograms showed a clear trend (Fig. 4I). For Q86, 2.5±5.9% of virions
242   were mature (N=7 tomograms), whereas 46±46% of R86 virions were mature (N=7 tomograms), a
243   significantly higher percentage (p=0.02, unpaired t test). Wildtype LGTV was intermediate to the two
244   recombinant viruses, with 14±25% mature virions. Taken together, a single residue in the distal part of
245   the TBEV furin site affects prM cleavage rates by furin and PC1/3, mean survival in
246   immunocompromised mice, and particle maturation in areas near ROs.

247

A protein complex connects the replication organelle to an apposed ER membrane

249   A recurring feature in the cryo-electron tomograms was the close proximity of a second ER membrane
250   to the ER membrane containing the ROs (Figs. 1-2). We noticed that this was consistently mediated by
251   a protein complex present at the membrane neck of the replication organelle, connecting this
252   membrane to the adjacent, second ER membrane (Fig. 5A-D). While limited occurrences of these
253   complexes hindered structural analysis, they consistently appeared at the necks of both filled and
254   empty ROs (Fig. 5A-D). From volume estimates of individual complexes, we estimate their molecular
255   masses to 500±151 kDa (Fig. 5E). Interestingly, we observed similar-looking complexes connecting
256   the replication organelle to the site of immature particle budding in the neighboring ER cisterna (Fig.
257   5F-H). This observation suggests that this protein complex might play a role in coordinating the
258   packaging of newly synthesized viral RNA into nascent immature virions.

259

Cryo-ET reveals structural signatures of LGTV replication in *ex vivo* mouse brain

261   We next wished to explore if the structural features of LGTV replication that we observed in cell lines
262   can also be identified directly in a complex, infected tissue. To do so, we proceeded to set up a

7

263 workflow for cryo-ET of LGTV-infected mouse brain tissue. We based our approach on our recent
264 publication, in which we imaged entire, *ex vivo*, LGTV-infected brains from type I interferon receptor
265 knockout (*Ifnar*$^{-/-}$) mice using fluorescence optical projection tomography[39]. In the 3D volumes of
266 infected brains, immunofluorescence staining against LGTV NS5 protein was particularly strong in the
267 choroid plexus (ChP) regions of the brain (Fig. 6A). ChP is an anatomical substructure responsible for
268 secreting cerebrospinal fluid (CSF) into the ventricles, and as such it interfaces both with the blood
269 and the CSF-filled ventricles (Fig. 6A). The ventricular side of the CSF-producing ependymal cells is
270 covered with cilia and microvilli (Fig. 6A). Based on the consistently strong infection of the ChP, we
271 developed a cryo-ET workflow for imaging ChP that was surgically removed from infected brains *post*
272 *mortem*. Due to the thickness of this sample, we opted for vitrification through high-pressure freezing.
273 The vitrified tissue was trimmed using a cryo-ultramicrotome after which lamellas were milled in
274 place and subjected to cryo-ET (Fig. 6A). The tomograms of ChP revealed a multitude of subcellular
275 structures such as mitochondria, nuclear pore complexes and a centriole (Fig. S6A-B). In addition,
276 some tomograms contained virus-related features consistent with the observations in infected cell
277 lines. This included mature virus particles encapsulated in vesicles close to membranes containing
278 several ROs (Fig. 6B-D). Another tomogram contained a *bona fide* empty RO with seemingly thicker
279 membrane than its limiting ER membrane, mirroring the features seen in cellular tomograms (Fig. 6E-
280 F). Taken together, we present the first cryo-ET data on virus replication in brain tissue. The data
281 support our cell line-based findings of RO-proximal virion maturation, and the presence of empty
282 ROs, and provide a proof of principle that neurotropic virus replication can be studied by cryo-ET
283 directly in infected brain samples.

284

Discussion

286 Here, we present an *in situ* structural study of tick-borne flavivirus replication, using cryo-ET of
287 infected cells and mouse brains. Flaviviruses are part of the vast phylum *Kitrinoviricota*, which is
288 characterized by ROs housed in membrane buds[40]. These viruses thus need to encode mechanisms for
289 remodeling host-cell membranes into a high-curvature bud, which is a high-energy and normally
290 transient membrane shape. However, the viruses need to stabilize this bud-shaped membrane
291 throughout hours of viral RNA replication. We recently showed that another genus of *Kitrinoviricota*,
292 alphaviruses, stabilize their RO membrane through a coat-free mechanism that involves bud neck
293 constraint by a viral protein complex, and inflation of the membrane bud by the intraluminal pressure
294 from the viral RNA[32]. With this mechanism, the size of the replication organelle is determined by the
295 amount of encapsulated RNA, and there are no membrane buds in the absence of intraluminal RNA.
296 Here, we show that flaviviruses employ a different mechanism to shape the RO membrane. A
297 membrane coat establishes a baseline RO size, allowing for the existence of ROs without intraluminal
298 RNA. The tomograms do not indicate an ordered protein coat lattice on the RO membrane, nor clear
299 individual protein densities, but it is possible that the curvature-generating proteins are too small
300 and/or irregularly distributed to be detected by cryo-ET. We suggest that a strong candidate for this RO
301 curvature generator is the 39 kDa, ER lumen-resident, non-structural protein NS1. NS1 is a peripheral
302 membrane protein that has been reported to remodel liposomes[41], and reshape the ER membrane when
303 overexpressed on its own[42]. The increase in RO size due to intraluminal RNA was back-calculated to
304 stem from the pressure of a single viral genomic RNA copy in dsRNA form (Fig. 2G, Fig. S2).
305 Alphavirus ROs also contain a single genome copy, indicating that this may be a conserved feature
306 across *Kitrinoviricota*[32]. Whether the smaller, empty ROs represent assembly intermediates,
307 disassembly intermediates, or dead-end, failed RO assembly events remains to be determined.

308 A close coupling of flavivirus genome replication and particle budding has been suggested by several
309 lines of evidence[14,18-20]. Our cryo-electron tomograms clearly resolved the maturation state of individual
310 virions, as supported by the good agreement between the cellular subtomogram averages and structures
311 of purified virions[23,25] (Fig. 3D-E, Fig. S4). The tomograms frequently revealed immature virions in the

312   immediate vicinity of ROs, sometimes in membrane compartments opposite to ROs (Figs. 3,6). The
313   observation of a ~500 kDa protein complex, connecting the membranes from which ROs and virions
314   form (Fig. 6), shows that flavivirus ROs have a "crown" or "neck complex" akin to those identified for
315   e.g. coronaviruses, nodaviruses and alphaviruses[30,32,43-50]. Indeed, of the seven flavivirus non-structural
316   proteins, four are integral membrane proteins of unknown structure and no known enzymatic function.
317   Thus, it is possible that these proteins server a structural role in organizing a membrane-connecting neck
318   complex that coordinates replication and assembly, but larger tomographic data sets would be required
319   to get a decisive subtomogram average from infected cells. Recent publications have highlighted the
320   potential in small-molecule antivirals that target non-enzymatic functions of flavivirus NS proteins[51-53].
321   These antivirals were discovered without structural insights into their target proteins, but it is possible
322   that the neck complex we identify here is their target. Either way, a more detailed understanding of the
323   neck complex structure and function may aid the design of improved antiviral strategies.

324   Contrary to the prevailing model, we observed that furin-dependent virus maturation takes place in the
325   immediate vicinity of ROs (Fig. 3). Thus, the entire sequence replication-assembly-maturation is more
326   closely colocalized than previously thought. The maturation compartments are distinct but intertwined
327   with ROs (Fig. 3), suggesting a revised model of flavivirus maturation, in which a virus-induced
328   reorganization of the secretory pathway places Golgi-like maturation compartments in the immediate
329   proximity of ROs. Studying naturally occurring furin site variants, we could show that a single residue
330   in the distal cleavage site affects the RO-proximal virion maturation, while having no effect on virus
331   release and only a minor effect on lethality in an immunocompromised mouse model (Fig. 4). This
332   suggests that the replication and infection of TBEV is robust to variations in its maturation pathway. A
333   further step towards bridging structural and organismal studies of flavivirus replication is taken by the
334   workflow we present for cryo-ET of infected *ex vivo* mouse brain tissue. Tomograms of infected choroid
335   plexus revealed clear structural signatures of ROs and clustering mature virions, similar to those in cell
336   lines (Fig. 7). While cryo-ET has recently been used to study Alzheimer's disease in human brain[54], our
337   data are, to the best of our knowledge, the first cryo-ET visualization of infection processes in the brain.
338   Future incorporation of novel lift-out and serial milling techniques into this workflow will allow for
339   faster acquisition of larger cryo-ET data sets on infected brains[55,56]. This may e.g. enable structural
340   analysis of virion maturation in brain samples, and comparison of replication features between different
341   knock-out mice. In conclusion, our study identifies several novel structural features of tick-borne
342   flavivirus replication, and places them in a cellular context that reveals a high degree of spatial
343   coordination of genome replication, virion assembly and virion maturation.

344

Materials and Methods

Cell line and culturing

347   The human A549 lung epithelial cell line was grown in DMEM medium supplemented with 10% fetal
348   bovine serum (FBS) and Penicillin Streptomycin GlutaMAX Supplement (Gibco) at 37°C in a 5%
349   CO_2 environment.

350

Sample preparation for cryo-electron tomography of cells

352   Ultrafoil Au R2/2 200 mesh grids (200 mesh, Quantifoil Micro Tools GmbH) were glow discharged.
353   Under laminar flow the grids were dipped in ethanol before being placed in μ-Slide 8 Well Chamber
354   (IBIDI) wells. DMEM medium with 10% FBS was added to each well and incubated while cells were
355   being prepared. Fresh medium was added to wells and cells were seeded out at 1.5×10^4 cells/well. The
356   seeded cells were then placed in a 37°C, 5% CO_2 incubator for 24 h. The medium in the wells was then
357   replaced with serum-free DMEM and either Langat virus wildtype (LGTV), recombinant chimeric

358 R86, or recombinant chimeric Q86 added at an MOI of 20. The cells were incubated for one hour
359 before replacing the medium with 2% FBS in DMEM and left to incubate for 24 h. The medium was
360 replaced with fresh DMEM including 2% FBS before being taken for freezing. Plunge freezing into an
361 ethane/propane mix was performed with a Vitrobot (ThermoFisher Scientific) at 22°C, 100%
362 humidity, blotting time of 5 s, and blot force of -5.

363

364 **Preparation of cryo-lamellas of cells**

365 Lamellas were milled from plunge-frozen cells using the Scios dual beam FIB/SEM microscope
366 (ThermoFisher Scientific). Samples were first coated with a platinum layer using the gas injection
367 system (GIS, ThermoFisher Scientific) operated at 26°C and 12 mm working distance for 10 seconds
368 per grid. Lamella were milled at an angle range of 16°-20°. The cells were milled stepwise using a
369 gallium beam at 30kV with decreasing current starting at 0.5 nA for rough milling and ending at 0.03
370 nA for final polishing of the lamella. Lamellas were milled to a nominal 200 nm thickness and stored
371 in liquid nitrogen for less than a week before being loaded into a Titan Krios (ThermoFisher
372 Scientific) for data collection.

373

374 **Cryo-ET data collection on cells**

375 Data were collected using a Titan Krios (ThermoFisher Scientific) at 300 kV in parallel illumination
376 mode. Tilt series acquisition was done using SerialEM[57] on a K2 Summit detector (Gatan, Pleasanton,
377 CA) in super-resolution mode. The K2 Summit detector was fitted with a BioQuantum energy filter
378 (Gatan, Pleasanton, CA) operated with a 20eV width silt. Areas to be imaged were selected from low-
379 magnification overview images based on the presence of convoluted cytoplasmic membranes. Tilt
380 series were collected using a 100 µm objective aperture and a 70 µm condenser 2 aperture, after
381 coma-free alignment done using Sherpa (ThermoFisher Scientific). Tilt series were collected using the
382 dose-symmetric scheme with a starting angle of -13° to account for lamella pre tilt. The parameters
383 used for acquisition were: 33,000x nominal magnification with a corresponding object pixel size of
384 2.145 Å in super-resolution mode, a tilt range of typically -50° to +50°, defocus between -3 µm and -5
385 µm, tilt increment of 2°, and a total electron dose of 110 e/ $Å^2$.

386

387 **Image Processing**

388 Motion correction, tilt series alignment, CTF estimation and correction, and tomogram reconstruction
389 was performed as described previously[58], using MotionCor2[59] with Fourier binning of 2, IMOD[60,61],
390 and CTFFIND4[62]. For visualization and segmentation, tomograms were 3 times binned using IMOD,
391 resulting in a pixel size of 12.87 Å. Tomograms were denoised using cryoCARE[63] or IsoNet[64],
392 occasionally combined with a non-local means filter as implemented in Amira (Thermo Fisher
393 Scientific). Segmentation of tomograms was performed in Amira, with initial membrane tracing and
394 segmentation done using MemBrain V2[65]. Subtomogram averages of mature and immature virus
395 particles were incorporated into segmentation using UCSF Chimera[66]. Amira was used for counting of
396 visually recognizable features (empty and filled ROs, immature and mature particles), measurements
397 of the distances between them, and the volume of the neck complex densities. The neck complex
398 volumes were converted to estimated molecular masses assuming assuming 825 Da/nm^3 [67].

399

400 **Subtomogram averaging of virions**

401 From tomograms generated with WARP[68] at 10Å/px object pixel size, immature and mature particles
402 were manually picked based on their clearly distinguishable appearance. 84 immature and 51 mature
403 particles were extracted from 11 and 3 tomograms, respectively, with a box size of 80*80*80 voxels.
404 Subtomogram averaging was done in Dynamo[69,70], following the same procedure for both the
405 immature and mature data sets. Initially, all particles were translationally and rotationally aligned to a
406 single, high-contrast particle from the respective data sets, without symmetrization. These C1 averages
407 were manually rotated and saved in UCSF Chimera[66] to approximately fit Dynamo's icosahedral
408 convention, after which they were used as a template for a Gold-standard alignment with imposed
409 icosahedral symmetry, using Dynamo's Adaptive bandpass Filtering function. Gold-standard Fourier
410 shell correlation curves estimated the resolution at a cutoff of 0.143 to 33 Å for the immature particles,
411 and 80Å for the mature particles, respectively. The final averages were filtered to this resolution and
412 masked using the spherical alignment mask.

413

414 **Estimating RO intraluminal pressure**
415 In recent work[32], we demonstrated the relation between the length of an RNA and the volume of the
416 surrounding spherule. Spherules with a volume of $V = 10^3 - 2 \cdot 10^3 nm^3$ contain $4 \cdot 10^3 - 10^4$ base
417 pairs (Fig. S2A), where the number of base pairs N is well described by

418 $$N = \frac{L_0}{l_{bp}}\left[1 + \frac{\sigma R_N^2}{\kappa} 2\left(\frac{3}{4\pi}\right)^{4/3}\left(\frac{V}{R_N^3}\right)^{4/3}\right], \tag{S1}$$

419 with $L_0 = 333nm$, $\sigma R_N^2/\kappa = 0.02$, $R_N = 9.6nm$ and the length per base pair $l_{bp} = 0.256nm$.
420 Furthermore, a theoretical model was used to determine the relationship between the scaled pressure
421 PR_N^3/κ and the scaled volume V/R_N^3 (Fig. S2B). Combining both results, we obtain a relation between
422 the pressure P and the number of base pairs N, which shows that an RNA with a length of $2 \cdot 10^3 -$
423 10^4 base pairs corresponds to a pressure of $10^{-3} - 10^{-4} k_B T nm^{-3}$ (Fig. S2C).
424

425 **Immunofluorescence staining**

426 Cells were grown on cover glasses and infected with LGTV as for cryo-ET. At 24 h p.i., cells were
427 fixed with 4% formaldehyde for 20 min at room temperature and then rinsed with PBS. The fixed cells
428 were permeabilized with 0.1% Triton X-100 in PBS for 10 min at room temperature and then rinsed
429 with PBS. The cells were then blocked with 2% BSA in PBS containing 0.05% Tween-20 (PBS-T) for
430 1 hour at RT. The cells were then stained with primary antibodies against furin (goat polyclonal,
431 dilution 1:50, Invitrogen), GM130 (mouse monoclonal clone 35/GM130, dilution 1:300, BD
432 Transduction) or dsRNA (mouse monoclonal clone J2, dilution 1:1000, Scicons, Nordic MUbio;
433 conjugated to allophycocyanin, Abcam) and secondary fluorescent antibodies (donkey anti-goat Alexa
434 Fluor 488, dilution 1:1000, Invitrogen; goat anti-mouse Alexa Fluor 568, dilution 1:1000, Invitrogen)
435 and DAPI diluted in blocking buffer for 1 hour each. Fluorescence images were acquired using a Leica
436 SP8 confocal microscope with a HC PL APO 63x/1.4 oil CS2 objective (Leica). Confocal fluorescence
437 images were analyzed using ImageJ Fiji software[71].

438

439 **Chimeric viruses**

440 A detailed description of chimeric LGTV (rLGTV[T:prME]) generation, rescue, and characterization can
441 be found in our recent manuscript[36]. In brief, the infectious clone of LGTV, strain TP21 (kind gift of
442 Prof. Andres Merits) was used as genetic background into which the prM and ecto-E from TBEV
443 strain 93/783 (GenBank: MT581212.1) was inserted. Point mutation resulting in the R86Q amino acid
444 substitution in the prM protein were introduced by overlapping PCR with primers; For: 5'
445 GGACGCTGTGGGAAAC_A_GGAAGGCTCACGGACA '3, Rev: 5'
446 TGTCCGTGAGCCTTCC_T_GTTTCCCACAGCGTCC 3' (Sigma-Aldrich). RNA was generated from
447 linearized DNA by in vitro transcription and transfected into BHK21 cells using Lipofectamine 2000

11

448 (Invitrogen). Supernatant from transfected cells was passaged once in A549 mitochondrial antiviral
449 signaling protein (*MAVS*$^{-/-}$) cells, confirmed by sequencing and used for all downstream experiments
450 without further passaging.

451

RNA isolation and qPCR

453 RNA was extracted from cell supernatant using Viral RNA kit (Qiagen) according to manufacturer's
454 instructions. The elution volume was kept constant and cDNA was subsequently synthetized from 10
455 µl of eluted RNA using high-capacity cDNA Reverse Transcription kit (Thermo Fisher). LGTV RNA
456 was quantified with qPCRBIO probe mix Hi-ROX (PCR Biosystems) and primers recognizing NS3[72]
457 on a StepOnePlus real-time PCR system (Applied Biosystems).

458

Western blot

460 At indicated time points, supernatant was collected and A549 cells infected with rLGTV$^{T:prME}$ R86 or
461 Q86 were lysed in 350 µl of lysis buffer (50 mM Tris-HCl pH7.5 + 150 mM NaCl + 0.1% Triton X-
462 100) complemented with 1x protease inhibitor (cOmplete™ ULTRA, Roche, Basel, Switzerland) on
463 ice for 20 min. Following lysis, cellular debris was removed by centrifugation at 14,000 g for 10 min
464 at 4°C. Supernatant or pre-cleared cell lysate was mixed with Laemmli buffer to final concentration 1x
465 and boiled at 95°C for 5 min. Proteins were separated by standard SDS-PAGE and transferred to an
466 Immobilon®-P PVDF Membrane (GE Healthcare, Chicago, IL, USA). Blots were blocked overnight
467 at 4°C in blocking buffer (PBS + 0.05 % Tween 20 + 2% Amersham ECL Prime Blocking Reagent;
468 Cytiva), stained with primary antibodies against NS3[73] (chicken polyclonal, diluted 1:1500), tubulin
469 (rabbit polyclonal, diluted 1:4000, Abcam-ab6046) or M[74] (in-house rabbit polyclonal serum, diluted
470 1:500) overnight at 4°C followed by secondary antibodies (goat anti-chicken Alexa-555, donkey anti-
471 rabbit Alexa-647 (dilution 1:2500, Invitrogen, Waltham, MA, USA) for 1 h at room temperature. Blots
472 were visualized on Amersham™ Imager 680 (GE Healthcare).

473

Enzymatic assays

475 Synthetic peptides (Biomatik) corresponding to the P13 to P'1 residues of prM from TBEV strain Torö
476 (Dabcyl-GRCGKQEGSRTRRG-E(EDANS)) and 93/783 (Dabcyl-GRCGK<u>R</u>EGSRTRRG-
477 E(EDANS)) or corresponding peptides with an impaired furin recognition site (Dabcyl-
478 GRCGKREGSRTRAG-E(EDANS), Dabcyl-GRCGKQEGSRTRAG-E(EDANS)) was used as
479 substrate. Cleavage efficiency was assayed using an adapted fluorogenic peptide assay[75]. For furin, 3
480 U furin (Thermo Fisher, Waltham, MA, USA) was mixed with 100 µM of substrate in a total volume
481 of 100 µl reaction buffer (100 mM HEPES pH7.5 + 1 mM CaCl2 + 0.5% Triton X-100) at 30°C for
482 3h. For proprotein convertase 1/3 (PC1/3), 1 µg recombinant human PC1/3 (R&D Systems,
483 Minneapolis, MN, USA) was mixed with 100 µM of substrate in a total volume of 100 µl reaction
484 buffer (25 mM MES pH 6.0 + 5 mM CaCl2 + 1% (w/v) Brij-35) at 37°C for 1h. The emission at 490
485 nm measured every 3 min and the average rate calculated by linear regression.

486

Virus infection of mice

488 All animal experiments were conducted at the Umeå Centre for Comparative Biology (UCCB), under
489 approval from the regional Animal Research Ethics Committee of Northern Norrland and the Swedish
490 Board of Agriculture, ethical permit A9-2018, A41-2019, and conducted as described previously[39,72].
491 Briefly, *Mavs*$^{-/-}$ mice in C57BL/6 background (kind gift of Nelson O Gekara, Umeå University) were

492 infected by intraperitoneal injection of 10^4 focus-forming units (FFU) or intracranial injection of 10^2
493 FFU of rLGTV[T:prME] R86 or Q86 diluted in PBS. *Ifnar*^{−/−} mice were intracranially inoculated with 10^4
494 FFU of LGTV and sacrificed when they developed either one pre-defined severe sign or at least three
495 milder signs. Mice were monitored for symptoms of disease and euthanized as previously described
496 criteria for humane endpoint[39].

497

Cryo-ET of LGTV-infected mouse brain tissue

499 Based on optical projection tomography that visualized the infection distribution in entire, *ex vivo*
500 brains[39], choroid plexuses were surgically removed from brains of LGTV-infected *Ifnar*^{−/−} mice *post*
501 *mortem*. The choroid plexuses were perfused with ice-cold phosphate-buffered saline (PBS) and
502 rapidly transferred to ice-cold artificial CSF[76]. Just prior to high-pressure freezing, the tissue was
503 placed in a 3 mm copper high-pressure freezing carrier (Wohlwend) which can be clipped into an
504 Autogrid. The sample was covered with a 20% dextran solution in PBS as cryoprotectant and covered
505 with a sapphire disk. The assembled carrier was rapidly vitrified using a Leica EM HPM100 high-
506 pressure freezer. The frozen carrier was trimmed at cryogenic temperatures using a Leica EM FC7
507 cryo-ultramicrotome with a diamond knife. The copper carrier was trimmed to leave a flat tissue
508 sample on the carrier, measuring 100 μm in width, 20 μm in thickness, and 30 μm in depth[77]. Frozen
509 carriers were clipped into Autogrids (ThermoFisher) prior to cryo-FIB milling with a Scios dual-beam
510 FIB/SEM microscope (ThermoFisher Scientific).

511 The sample was coated with a protective platinum layer using a gas injection system for 15 seconds at
512 a working distance of 7 mm. The cryostage was tilted at an angle of approximately 10° for milling. A
513 rough milling was initially performed with an ion beam accelerating voltage of 30 kV and a current
514 ranging from 0.79 to 2.5 nA to reach a thickness of 1 μm. Additionally, the two sides of the lamella
515 were milled above and below to allow cryo-ET data collection by preventing the thick edges of the
516 tissue from obstructing transmission EM imaging[77]. After rough milling, one edge of the lamella was
517 detached from the main platform to relieve stress. When the lamella reached a thickness of
518 approximately 1 μm, the ion beam current was lowered to 80 to 230 pA for fine milling, resulting in a
519 final lamella thickness of around 200 nm. SerialEM was used to collect tilt series data with tilt angles
520 ranging from 40° to -40° in 2° increments. The total electron dose for a single tilt series was
521 approximately 100 e-/Å², with defocus between -5 and -10 μm. Tomograms were generated as
522 described above for cells.

523

Statistics and reproducibility

525 Data and statistical analysis were performed using Prism (GraphPad Software Inc., USA). Details
526 about replicates, statistical test used, exact values of n, what n represents, and dispersion and precision
527 measures used can be found in figures and corresponding figure legends. Values of $p < 0.05$ were
528 considered significant. All tomograms shown are representative of larger data sets as indicated in
529 Table 1.

530

Data availability

534

Acknowledgements

552

Figures and Tables

Figure 1: *In situ* cryo-ET uncovers two states of Langat virus replication organelles. (A) Slice through a tomogram of FIB milled LGTV-infected cell showing viral ROs enclosed within the ER with an immature virion (orange arrow). (B-C) Close up views of the outlined framed region in (A) at their respective Z heights in the tomogram. (A-C) White arrows indicate empty ROs. (D) Segmentation of the tomogram in (A), with color schemes defined for each structure. The immature virion is represented by a subtomogram average. (E) Representative examples of empty and filled viral RO observed in cryo-tomograms of milled LGTV-infected cells. (F) Percentage of filled ROs observed in 23 tomograms of LGTV-infected cells. (G) Size distribution of empty (n=25) and filled (n=63) RO observed in tomograms. The inset represents the different sizes of viral spherules observed in the tomograms. (F-G) Red lines represent the average, each dot corresponds to one analyzed tomogram (see also Table 1). Statistical significance by unpaired two-tailed Student's t test: ****$p < 0.0001$. Scale bars 100 nm.

15
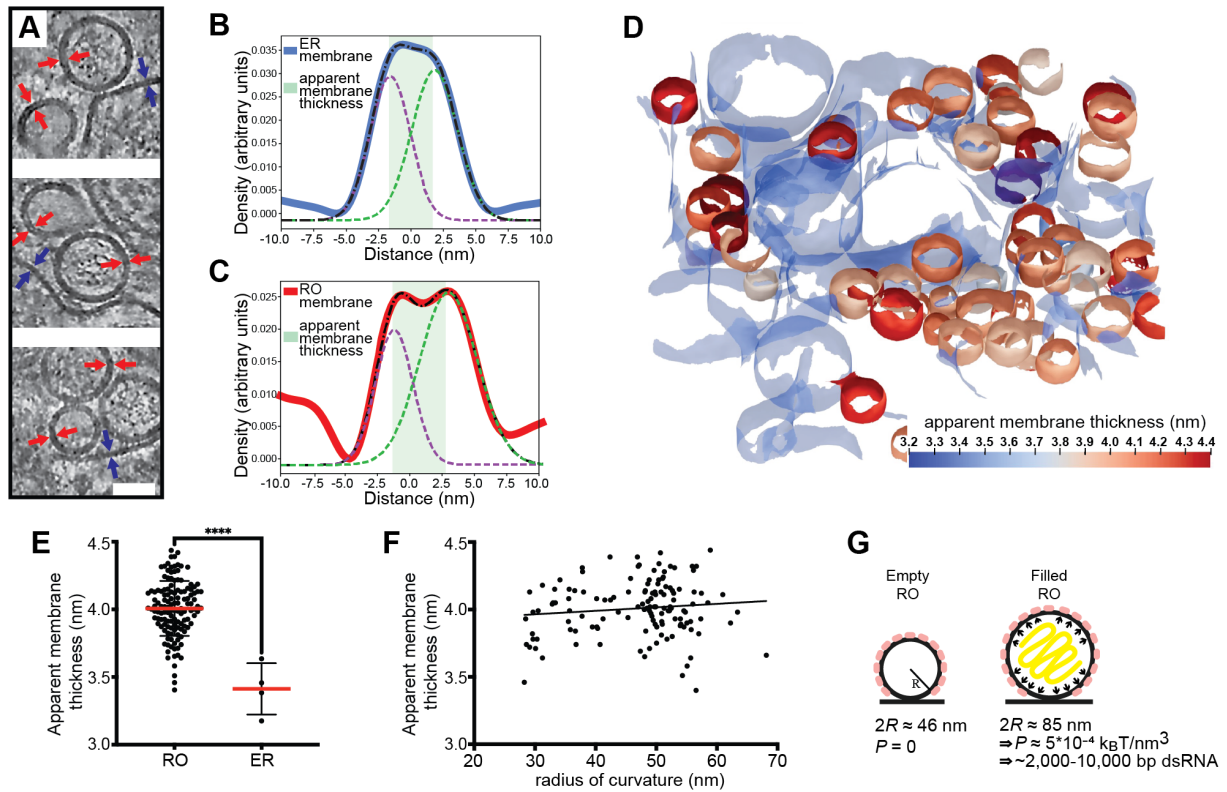
Figure 2: The influence of a membrane coat and viral RNA in shaping the replication organelles.
(A) Slices through tomograms of empty and filled ROs in LGTV-infected cells. Blue and red arrows indicate the thickness of the ER and RO membranes, respectively. Scale bar, 50 nm. (B-C) Membrane thickness estimation by dual Gaussian fitting to radial density plots through a representative ER membrane (B) and RO membrane (C). Solid lines, membrane density profile; dashed lines, fitted composite and dual Gaussian; shaded area, estimated thickness. (D) ER and ROs membranes from a representative tomogram of an LGTV-infected cell, color coded by apparent membrane thickness. ER membrane is partially transparent. (E) Apparent membrane thickness quantification in four tomograms of LGTV-infected cells, comparing individual ROs (n=132) and the surrounding ER (n=4). Red lines, average. Statistical significance by unpaired two-tailed Student's t test: ****p < 0.0001. (F) Relationship between radius of curvature and apparent membrane thickness for individual ROs (n=132 from six tomograms). (G) Model of the mechanisms determining viral RO size. Two RO states exist in infected cells: empty ROs with a baseline size set independent of luminal RNA, and filled ROs, whose larger size is due to intraluminal pressure from ~2,000-10,000 bp dsRNA.

16
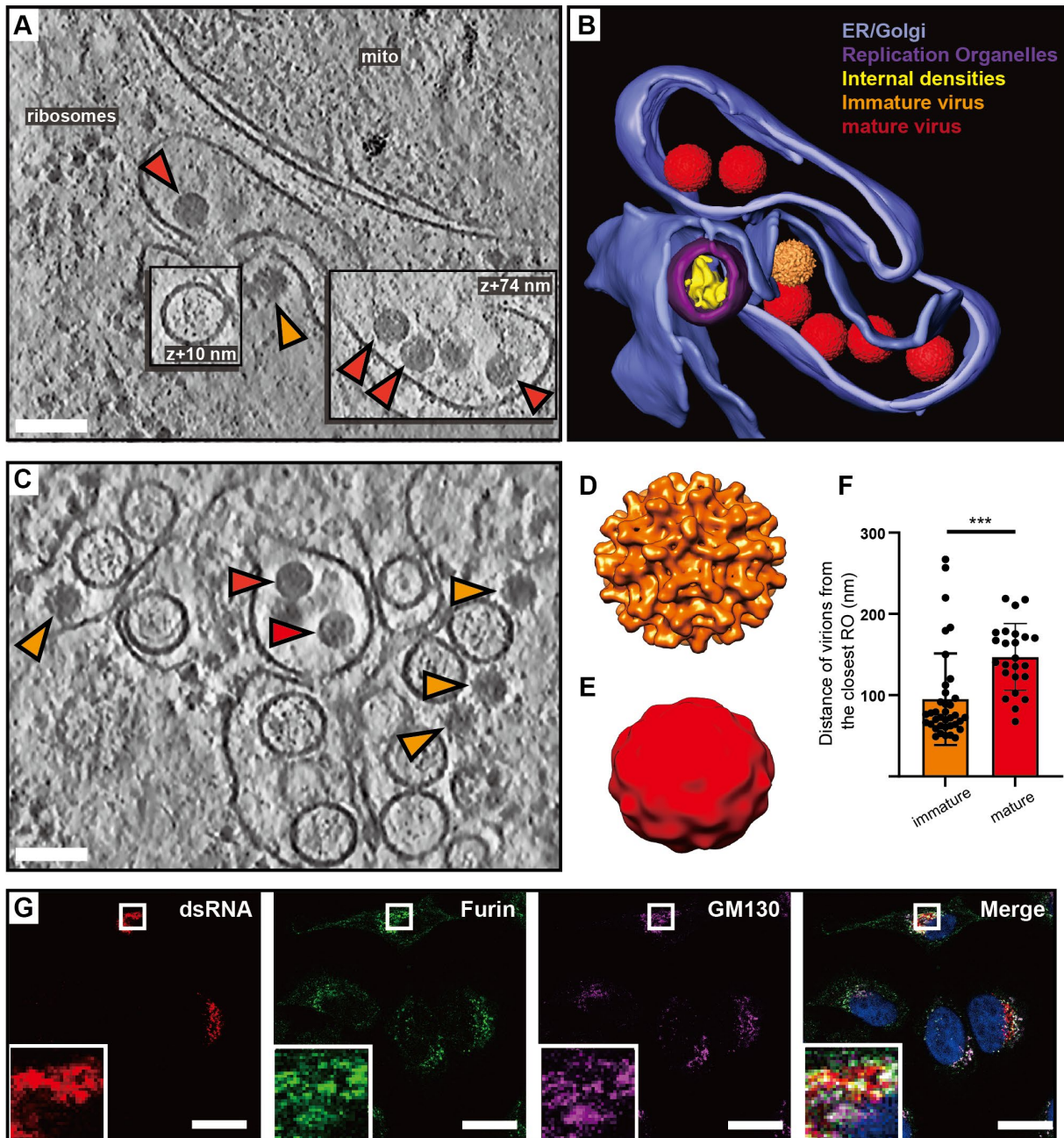
Figure 3: Virions form and mature in the immediate vicinity of replication organelles. (A) Slice through tomogram of LGTV-infected cell showing an immature virion budding across from a RO (orange arrow), and mature virions (red arrows) in adjacent membranes. (B) Segmentation of the tomogram in (A), with color labels defined for each structure. (C) Slice through tomogram of LGTV-infected showing mature (red arrows) and immature (orange arrows) LGTV virions observed near the viral RO. (D-E) Subtomogram averages of immature (D) and mature (E) LGTV from cellular tomograms. (F) The distance from immature (n=37) and mature (n=24) virions to the closest RO, from five tomograms. Statistical significance by unpaired two-tailed Student's t test: ****$p < 0.005$. (G) Representative immunofluorescence micrograph of dsRNA, furin and Golgi marker GM130 in LGTV-infected cells at 24 h p.i. Rightmost panel: merge including DAPI-staining of nuclei (blue). Scale bars 100 nm (A,C), 5 μm (G).

17
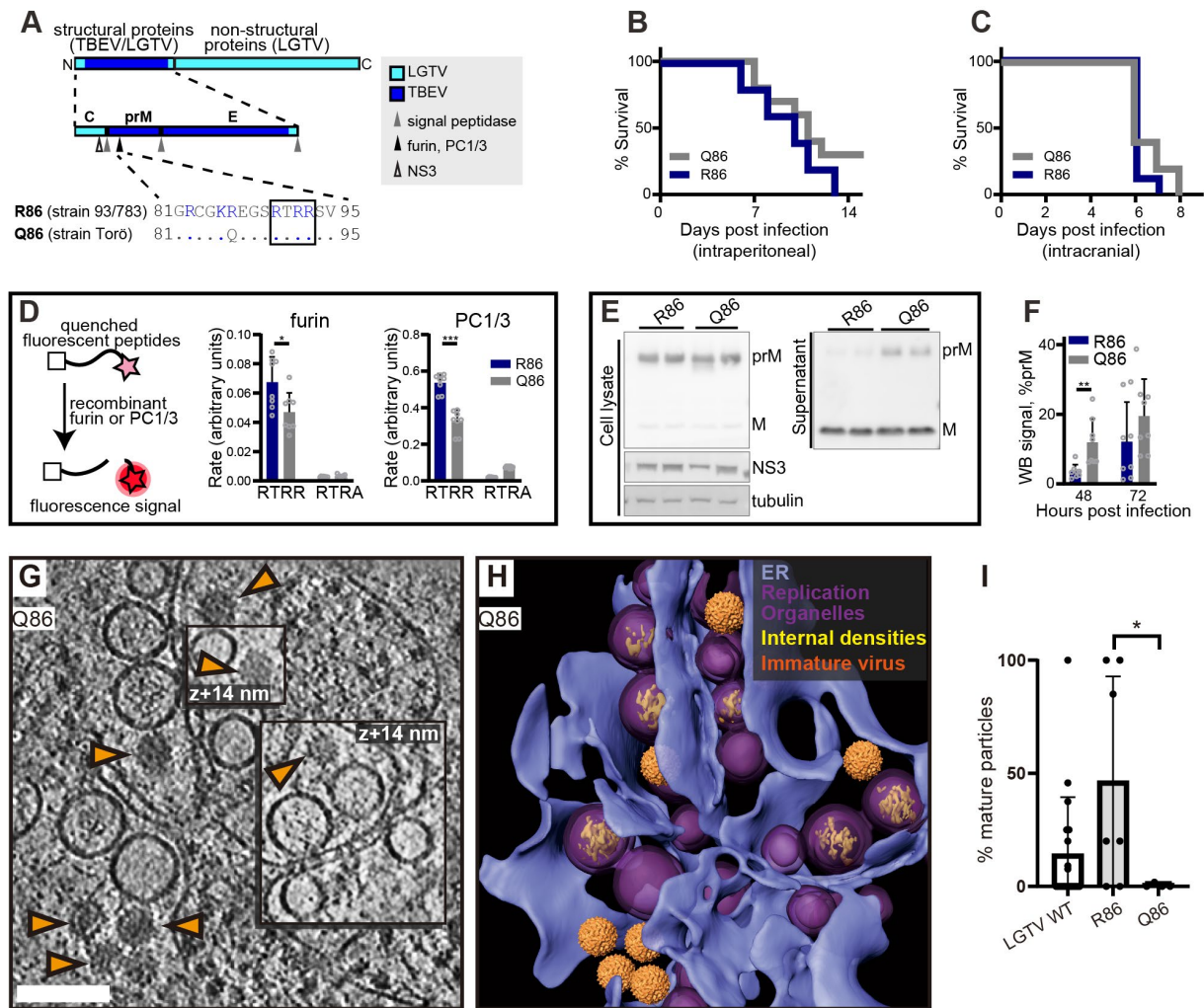
Figure 4: The TBEV furin site variants R86 and Q86 differ in cleavage efficiency and replication organelle-proximal virion maturation. (A) The polyprotein of a chimeric LGTV with prM and ecto-E from TBEV strain 93/783, as color coded. Recognition sites for viral and cellular proteases are shown within the structural protein region, and the furin site sequences from TBEV strains 93/783 and Torö are shown highlighting the difference at position 86 (., identical sequence). (B) Percentage survival of $Ips1^{-/-}$ mice infected intraperitoneally with 10^4 FFU with chimeric LGTV R86 (n=5) or Q86 (n=10). (C) As (B), for but $Ips1^{-/-}$ mice infected intracranially with 10^2 FFU (n=9, R86 and n=10, Q86). (D) Enzymatic cleavage using recombinant furin or PC1/3 with peptides corresponding to furin site sequences in (A) (RTRR), or peptides with impaired furin sites (RTRA). Data from four independent experiments performed in duplicates are shown, with mean values and standard deviation. (E) prM and M protein levels in cell lysates and supernatant 48 h.p.i. visualized by immunoblotting. Viral NS3 and cellular tubulin included as infection and loading control. Representative blots are shown. (F) Ratio of prM/M intensity quantified in supernatants at 48 and 72 h.p.i. Data from four independent experiments performed in duplicates are shown, with mean values and SD. (G) Slice through tomogram of chimeric LGTV Q86-infected cell showing a predominance of immature virions (orange arrows) within the cytoplasm. Scale bar 100 nm. (H) segmentation of the tomogram in (A), with color labels defined for each structure. (I) Percentage of mature virions in the tomograms of LGTV WT (n=19), chimeric LGTV R86 (n=6), LGTV Q86- infected cells (n=4). (D,F,I) Statistical significance by unpaired two-tailed Student's t test: *p<0.05, **p<0.01, ***p < 0.001.

18
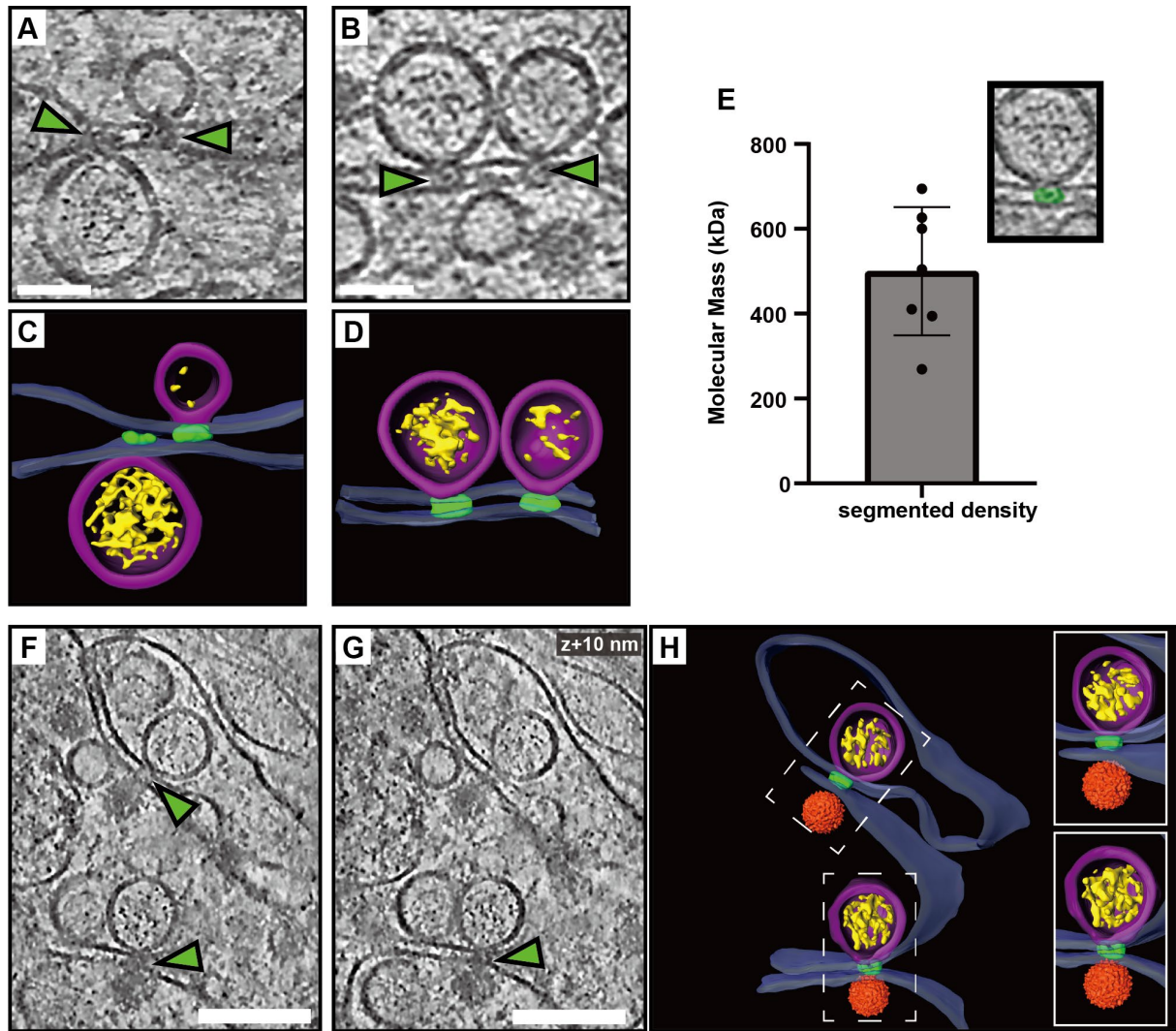
Figure 5: A protein complex zippers replication organelles to an apposed ER membrane. (A-B) Slices through tomograms of LGTV-infected cells showing complexes (green arrows) located at the neck of the ROs, connecting them to the adjacent ER membrane. (C-D) Segmentation of the tomograms in (A-B). (E) Estimated molecular masses of the complex (n=7). (F-G) Slices through the same tomogram at two different Z heights, showing complexes linking the RO to the site of virus assembly (green arrows). (H) Segmentation of the tomogram shown in (F-G). (C-D,H) Blue, ER membrane; purple, RO; yellow, luminal densities; green, neck complex; orange, immature virions. Scale bars, 100 nm.
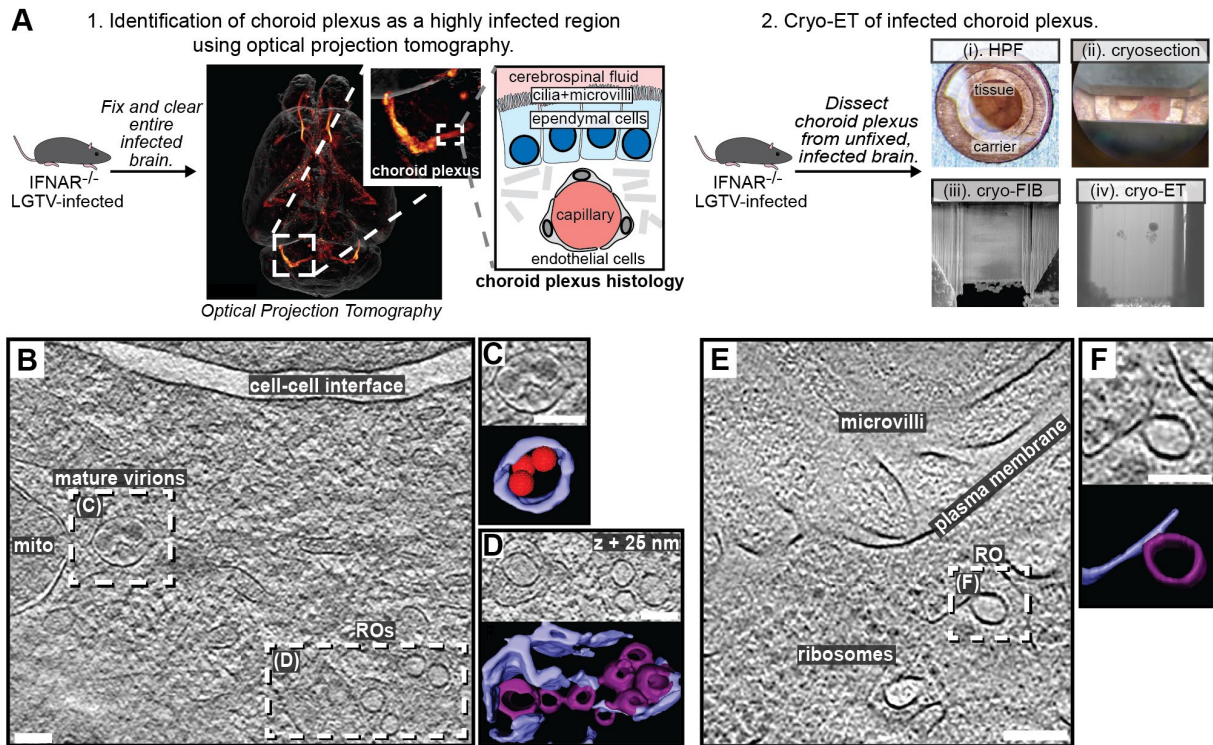
19

Figure 6: LGTV replication visualized in *ex vivo* mouse brain using cryo-ET. (A) Workflow for cryo-ET of *ex vivo* mouse brain. LGTV-infected brains from *Ifnar⁻/⁻* mice were processed differently based on the imaging method. 1. Fixed and cleared brains were immunostained for the viral protein NS5 (orange/red) and imaged using optical projection tomography. Zoomed insets show infected regions of the choroid plexus, and its anatomy. 2. For cryo-ET, the choroid plexus from unfixed and unstained LGTV-infected brains was (i) high-pressure frozen, (ii) trimmed using a cryo-ultramicrotome, (iii) FIB milled, and (iv) transferred to a cryo-TEM for cryo-ET. (B) Slice through a tomogram of LGTV-infected choroid plexus showing viral replication organelles and smooth virions in proximity, enclosed within membrane vesicles. (C-D) Close-up of the areas indicated in (B) along with their corresponding segmentations. (E) Slice through a tomogram of LGTV-infected choroid plexus showing a *bona fide* RO with a thicker membrane than the ER, consistent with observations from Fig. 2. (F) Close-up of the area indicated in (E) along with its corresponding segmentation. (B-F) Colors as in Fig. 3. Scale bars, 100 nm.

**Table 1. Number of tilt series recorded and tomograms analyzed.** "Number of tilt series" refers to the total number of tilt series recorded on a given sample. All of these tilt series were used to reconstruct tomograms, and the "number of tomograms with events" refers to the number of tomograms with virus replication-related events.

| sample	number of tilt series	number of tomograms with events
LGTV WT	51	23
rLGTV^T:prME R86	12	7
rLGTV^T:prME Q86	18	7
LGTV in *ex vivo* choroid plexus	45	8

20

648 **Supplementary figures and movies**
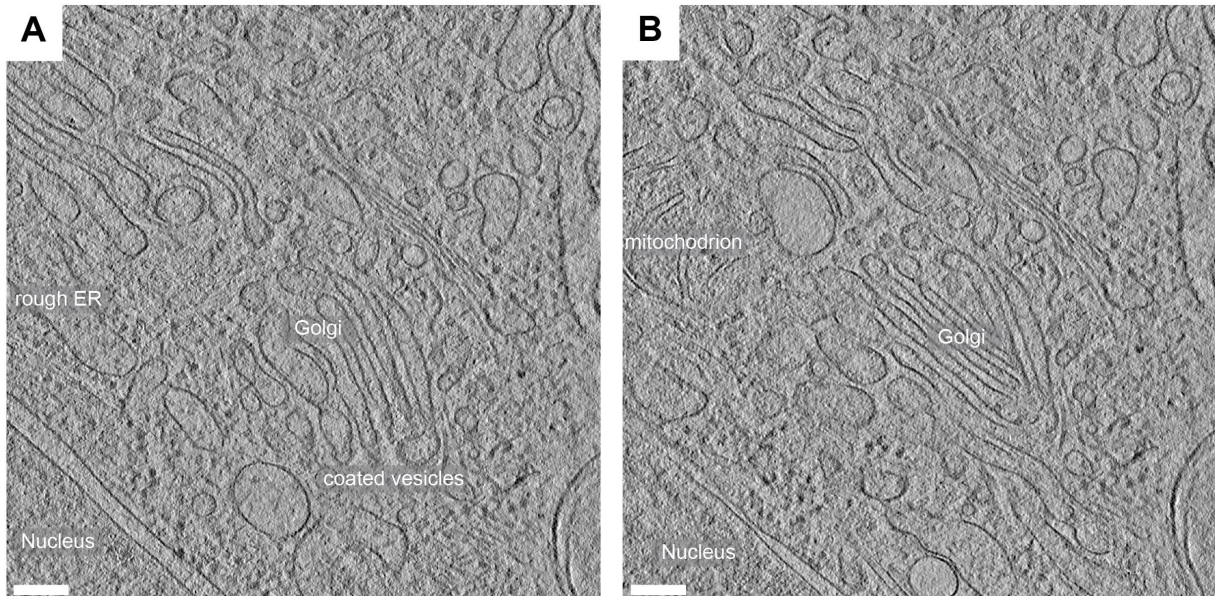
650 **Figure S1: cryo-ET of uninfected A549 cells. (A-B)** Slices from two tomograms of uninfected A549
651 cells reveal typical cytoplasmic features, as indicated, including a non-dilated ER and *bona fide* Golgi
652 cisternae with typical morphology. Scale bars,100 nm.
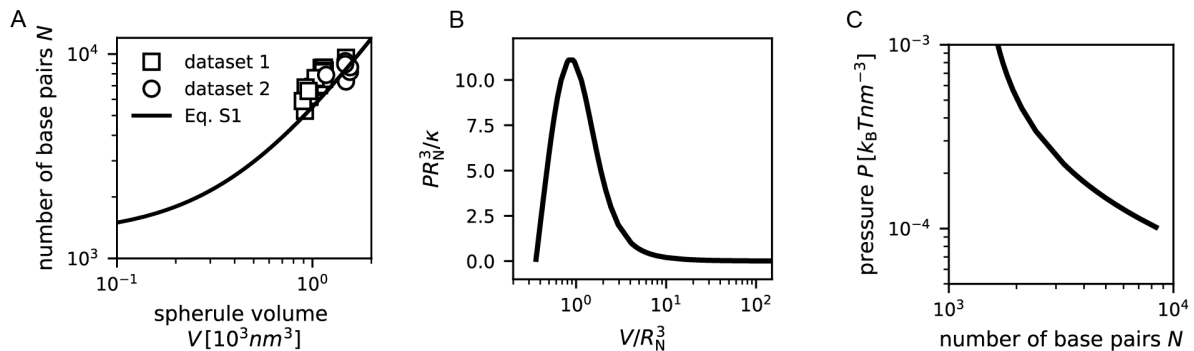
655 **Figure S2. Pressure exerted by an RNA strand.** (A) Relation between number of RNA base pairs
656 and RO volume. The data is reproduced from Laurent *et al*[32]. We note that in Laurent *et al*[32] the RNA
657 length is shown, while here the number of base pairs is shown, assuming an interbasepair distance of
658 2.56 Å. (B) Relation between the scaled pressure and the scaled volume. The details of the underlying
659 model are presented in Laurent *et al*[32]. (C) Relation between number of RNA base pairs N and
660 pressure P, where we use the results from (A-B) to convert the RO volume into number of RNA base
661 pairs.

21
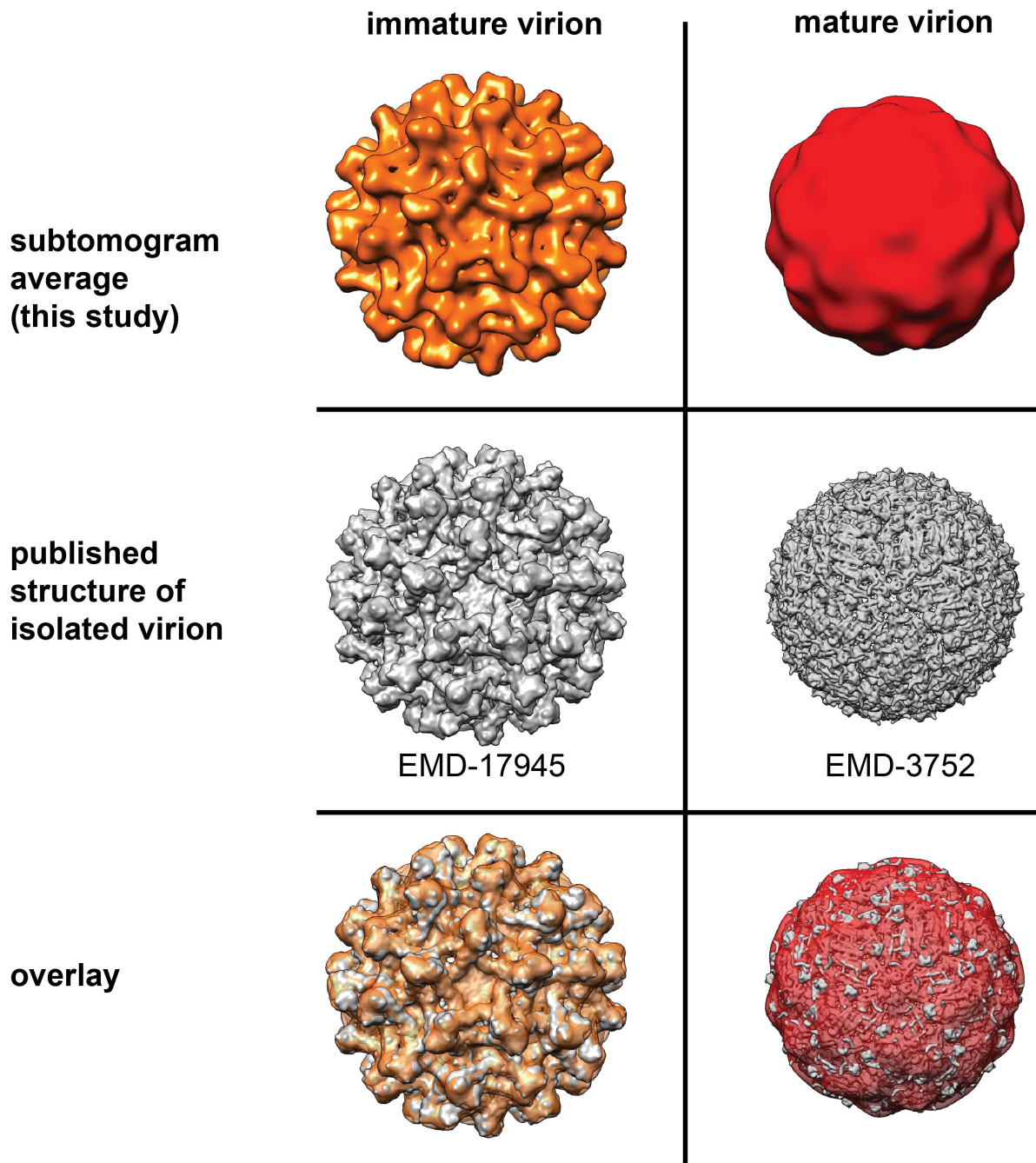
Figure S3: Comparison of cellular subtomogram averages with isolated virion structures. The cellular subtomogram averages from this study (top row) are compared to low-pass filtered published structures of immature and mature TBEV, from Fuzik *et al*[25] and Anastasina *et al*[23], respectively (mid row). The overlays (bottom row) were created using the Align to Volume command, and are shown with the subtomogram averages in semi-transparent surface representation.
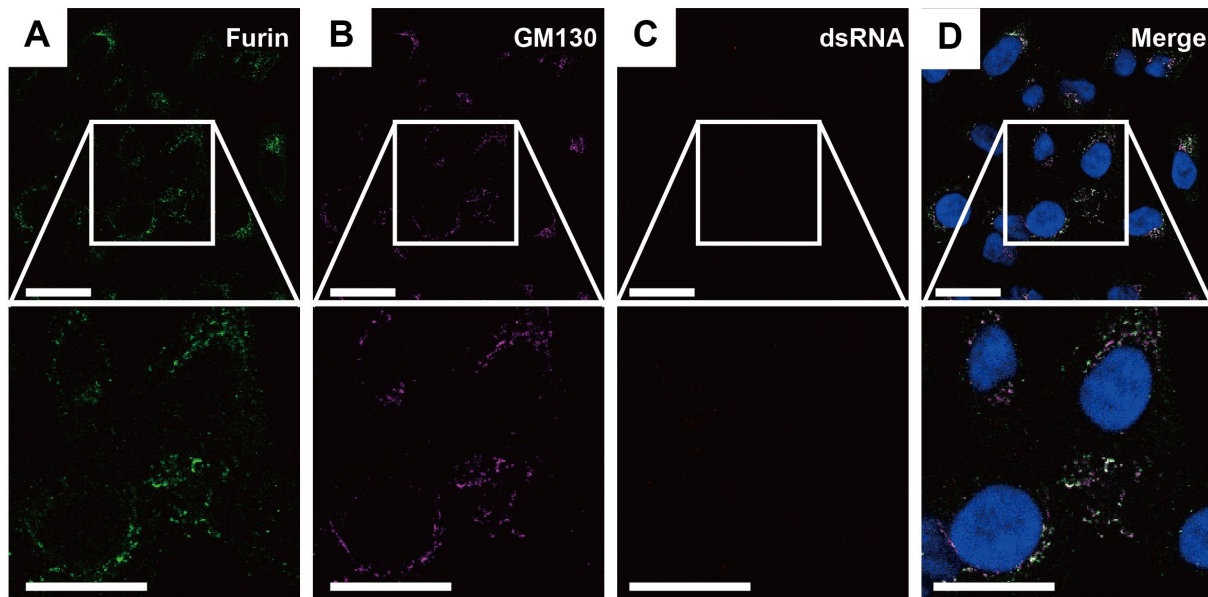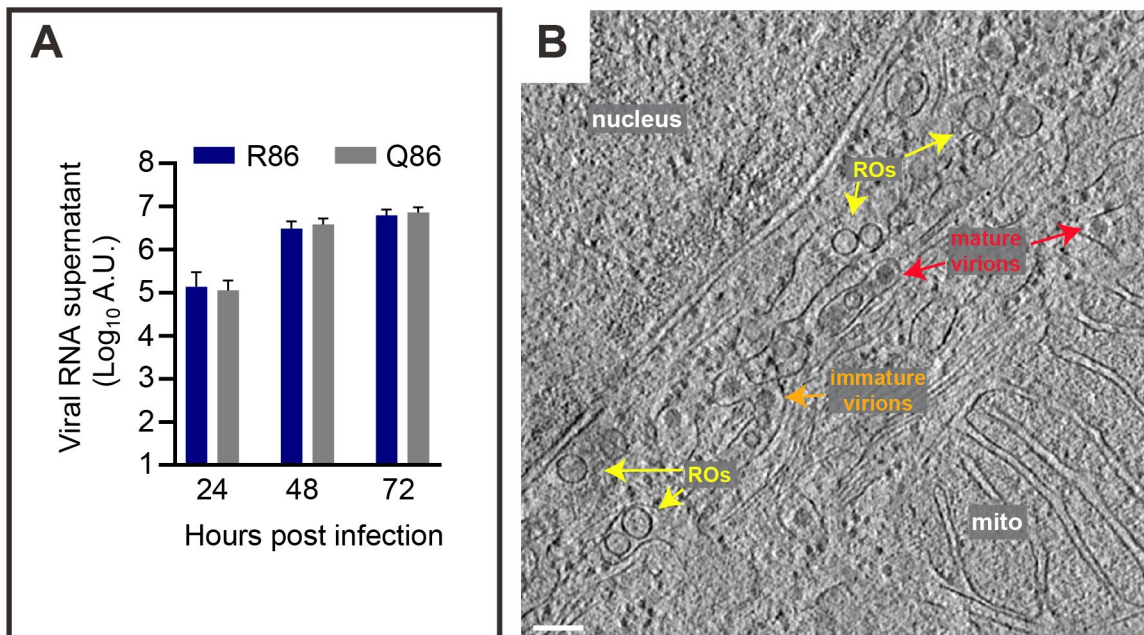
Figure S4: Furin localization in uninfected cells. Immunofluorescence microscopy of uninfected cells showing furin (A) and Golgi marker GM130 (B) and their colocalization in the absence of viral infection (D). Additional channels contain dsRNA staining (C) and DAPI staining of cell nuclei (D). Scale bars, 10 μm.

Figure S5: Data on rLGTV$^{T:prME}$ Q86 and R86. (A) Growth kinetics of rLGTV$^{T:prME}$ R86 and Q86 upon infection of A549 at MOI 1, quantitated as the amount of viral RNA in supernatant per qPCR. (B) Slice from a tomogram of a cell infected with rLGTV$^{T:prME}$ R86 at 24 h p.i. showing various cytoplasmic and virus-related features, as indicated. Scale bar 100 nm.

23
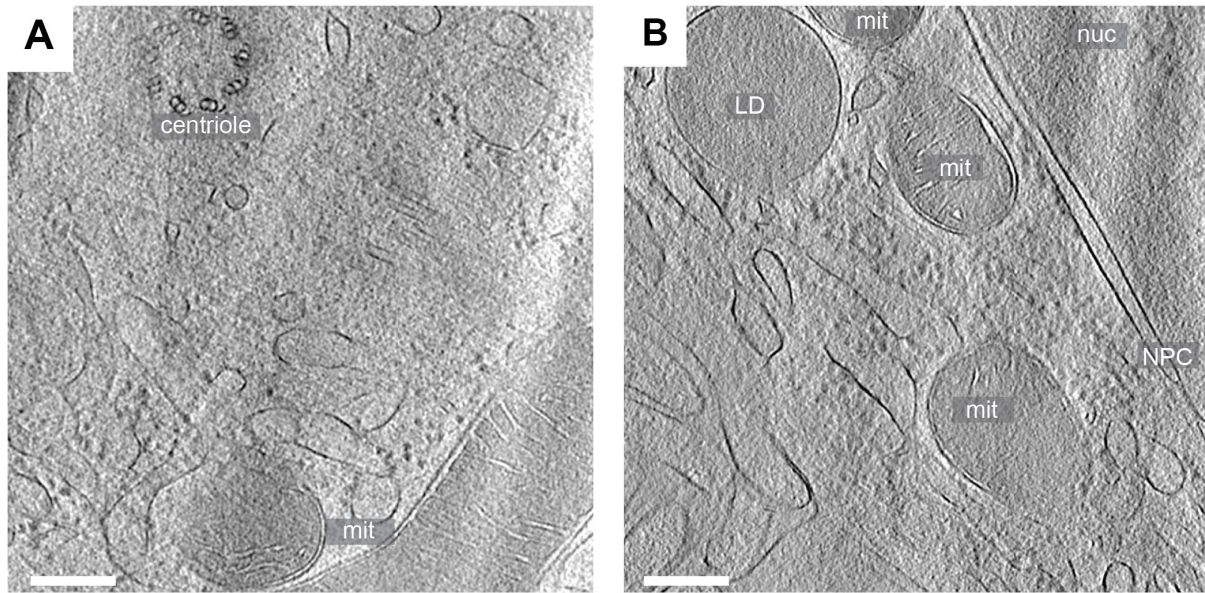
Figure S6: Features unrelated to infection in cryo-electron tomograms of *ex vivo* brain tissue. (A-B) Slices from two tomograms of high-pressure frozen choroid plexus from LGTV-infected *Ifnar*^{-/-} mice. The features indicated are a centriole, several mitochondria (mit), a lipid droplet (LD), the peripheral area of a nucleus (nuc) and the nuclear envelope including one nuclear pore complex (NPC). Scale bar, 100 nm.

Movie S1. Tomographic volume corresponding to the slice shown in Fig. 1A.

Movie S2. The segmentation shown in Fig. 1D.

Movie S3. Tomographic volume corresponding to the slice shown in Fig. 3A.

Movie S4. The segmentation shown in Fig. 3B.

Movie S5. Tomographic volume corresponding to the slice shown in Fig. 4G.

Movie S6. The segmentation shown in Fig. 4H.

Movie S7. Tomographic volume corresponding to the slices shown in Fig. 5F-G.

Movie S8. The segmentation shown in Fig. 5H.

Movie S9. Tomographic volume corresponding to the slice shown in Fig.6B.

References

1. Bhatt, S., Gething, P.W., Brady, O.J., Messina, J.P., Farlow, A.W., Moyes, C.L., Drake, J.M., Brownstein, J.S., Hoen, A.G., Sankoh, O., et al. (2013). The global distribution and burden of dengue. Nature *496*, 504-507. 10.1038/nature12060.

2. Chambers, T.J., and Diamond, M.S. (2003). Pathogenesis of flavivirus encephalitis. Adv Virus Res *60*, 273-342. 10.1016/s0065-3527(03)60008-4.

3. Ng, M.L. (1987). Ultrastructural studies of Kunjin virus-infected Aedes albopictus cells. J Gen Virol *68 (Pt 2)*, 577-582. 10.1099/0022-1317-68-2-577.

4. Ko, K.K., Igarashi, A., and Fukai, K. (1979). Electron microscopic observations on Aedes albopictus cells infected with dengue viruses. Arch Virol *62*, 41-52. 10.1007/BF01314902.

5. Neufeldt, C.J., Cortese, M., Acosta, E.G., and Bartenschlager, R. (2018). Rewiring cellular networks by members of the Flaviviridae family. Nature reviews *16*, 125-142. 10.1038/nrmicro.2017.170.

6. Aktepe, T.E., and Mackenzie, J.M. (2018). Shaping the flavivirus replication complex: It is curvaceous! Cell Microbiol *20*, e12884. 10.1111/cmi.12884.

7. Arakawa, M., and Morita, E. (2019). Flavivirus Replication Organelle Biogenesis in the Endoplasmic Reticulum: Comparison with Other Single-Stranded Positive-Sense RNA Viruses. Int J Mol Sci *20*. 10.3390/ijms20092336.

8. Ci, Y., and Shi, L. (2021). Compartmentalized replication organelle of flavivirus at the ER and the factors involved. Cell Mol Life Sci *78*, 4939-4954. 10.1007/s00018-021-03834-6.

9. van den Elsen, K., Quek, J.P., and Luo, D. (2021). Molecular Insights into the Flavivirus Replication Complex. Viruses *13*. 10.3390/v13060956.

10. Romero-Brey, I., Merz, A., Chiramel, A., Lee, J.Y., Chlanda, P., Haselman, U., Santarella-Mellwig, R., Habermann, A., Hoppe, S., Kallis, S., et al. (2012). Three-dimensional architecture and biogenesis of membrane structures associated with hepatitis C virus replication. PLoS Pathog *8*, e1003056. 10.1371/journal.ppat.1003056.

11. Yau, W.L., Nguyen-Dinh, V., Larsson, E., Lindqvist, R., Overby, A.K., and Lundmark, R. (2019). Model System for the Formation of Tick-Borne Encephalitis Virus Replication Compartments without Viral RNA Replication. J Virol *93*. 10.1128/JVI.00292-19.

12. Aktepe, T.E., Liebscher, S., Prier, J.E., Simmons, C.P., and Mackenzie, J.M. (2017). The Host Protein Reticulon 3.1A Is Utilized by Flaviviruses to Facilitate Membrane Remodelling. Cell Rep *21*, 1639-1654. 10.1016/j.celrep.2017.10.055.

13. Hoffmann, H.H., Schneider, W.M., Rozen-Gagnon, K., Miles, L.A., Schuster, F., Razooky, B., Jacobson, E., Wu, X., Yi, S., Rudin, C.M., et al. (2021). TMEM41B Is a Pan-flavivirus Host Factor. Cell *184*, 133-148 e120. 10.1016/j.cell.2020.12.005.

14. Welsch, S., Miller, S., Romero-Brey, I., Merz, A., Bleck, C.K., Walther, P., Fuller, S.D., Antony, C., Krijnse-Locker, J., and Bartenschlager, R. (2009). Composition and three-dimensional architecture of the dengue virus replication and assembly sites. Cell Host Microbe *5*, 365-375. 10.1016/j.chom.2009.03.007.

15. Junjhon, J., Pennington, J.G., Edwards, T.J., Perera, R., Lanman, J., and Kuhn, R.J. (2014). Ultrastructural characterization and three-dimensional architecture of replication sites in dengue virus-infected mosquito cells. J Virol *88*, 4687-4697. 10.1128/JVI.00118-14.

16. Offerdahl, D.K., Dorward, D.W., Hansen, B.T., and Bloom, M.E. (2012). A three-dimensional comparison of tick-borne flavivirus infection in mammalian and tick cell lines. PLoS One *7*, e47912. 10.1371/journal.pone.0047912.

17. Gillespie, L.K., Hoenen, A., Morgan, G., and Mackenzie, J.M. (2010). The endoplasmic reticulum provides the membrane platform for biogenesis of the flavivirus replication complex. J Virol *84*, 10438-10447. 10.1128/JVI.00986-10.

18. Apte-Sengupta, S., Sirohi, D., and Kuhn, R.J. (2014). Coupling of replication and assembly in flaviviruses. Curr Opin Virol *9*, 134-142. 10.1016/j.coviro.2014.09.020.

19. Kummerer, B.M., and Rice, C.M. (2002). Mutations in the yellow fever virus nonstructural protein NS2A selectively block production of infectious particles. J Virol *76*, 4773-4784. 10.1128/jvi.76.10.4773-4784.2002.

751 20. Xie, X., Zou, J., Zhang, X., Zhou, Y., Routh, A.L., Kang, C., Popov, V.L., Chen, X., Wang,
752   Q.Y., Dong, H., and Shi, P.Y. (2019). Dengue NS2A Protein Orchestrates Virus Assembly. Cell
753   Host Microbe *26*, 606-622 e608. 10.1016/j.chom.2019.09.015.
754 21. Överby, A.K., Popov, V.L., Niedrig, M., and Weber, F. (2010). Tick-borne encephalitis virus
755   delays interferon induction and hides its double-stranded RNA in intracellular membrane
756   vesicles. J Virol *84*, 8470-8483. 10.1128/JVI.00176-10.
757 22. Renner, M., Dejnirattisai, W., Carrique, L., Martin, I.S., Karia, D., Ilca, S.L., Ho, S.F.,
758   Kotecha, A., Keown, J.R., Mongkolsapaya, J., et al. (2021). Flavivirus maturation leads to the
759   formation of an occupied lipid pocket in the surface glycoproteins. Nature communications
760   *12*, 1238. 10.1038/s41467-021-21505-9.
761 23. Anastasina, M., Fuzik, T., Domanska, A., Pulkkinen, L.I.A., Smerdova, L., Formanova, P.P.,
762   Strakova, P., Novacek, J., Ruzek, D., Plevka, P., and Butcher, S.J. (2024). The structure of
763   immature tick-borne encephalitis virus supports the collapse model of flavivirus maturation.
764   Sci Adv *10*, eadl1888. 10.1126/sciadv.adl1888.
765 24. Newton, N.D., Hardy, J.M., Modhiran, N., Hugo, L.E., Amarilla, A.A., Bibby, S., Venugopal,
766   H., Harrison, J.J., Traves, R.J., Hall, R.A., et al. (2021). The structure of an infectious
767   immature flavivirus redefines viral architecture and maturation. Sci Adv *7*.
768   10.1126/sciadv.abe4507.
769 25. Fuzik, T., Formanova, P., Ruzek, D., Yoshii, K., Niedrig, M., and Plevka, P. (2018). Structure
770   of tick-borne encephalitis virus and its neutralization by a monoclonal antibody. Nature
771   communications *9*, 436. 10.1038/s41467-018-02882-0.
772 26. Kuhn, R.J., Zhang, W., Rossmann, M.G., Pletnev, S.V., Corver, J., Lenches, E., Jones, C.T.,
773   Mukhopadhyay, S., Chipman, P.R., Strauss, E.G., et al. (2002). Structure of dengue virus:
774   implications for flavivirus organization, maturation, and fusion. Cell *108*, 717-725.
775   10.1016/s0092-8674(02)00660-8.
776 27. Quemin, E.R.J., Machala, E.A., Vollmer, B., Prazak, V., Vasishtan, D., Rosch, R., Grange, M.,
777   Franken, L.E., Baker, L.A., and Grunewald, K. (2020). Cellular Electron Cryo-Tomography to
778   Study Virus-Host Interactions. Annu Rev Virol *7*, 239-262. 10.1146/annurev-virology-021920-
779   115935.
780 28. Nishikiori, M., den Boon, J.A., Unchwaniwala, N., and Ahlquist, P. (2022). Crowning Touches
781   in Positive-Strand RNA Virus Genome Replication Complex Structure and Function. Annu
782   Rev Virol *9*, 193-212. 10.1146/annurev-virology-092920-021307.
783 29. Hong, Y., Song, Y., Zhang, Z., and Li, S. (2023). Cryo-Electron Tomography: The Resolution
784   Revolution and a Surge of In Situ Virological Discoveries. Annu Rev Biophys *52*, 339-360.
785   10.1146/annurev-biophys-092022-100958.
786 30. Zimmermann, L., Zhao, X., Makroczyova, J., Wachsmuth-Melm, M., Prasad, V., Hensel, Z.,
787   Bartenschlager, R., and Chlanda, P. (2023). SARS-CoV-2 nsp3 and nsp4 are minimal
788   constituents of a pore spanning replication organelle. Nature communications *14*, 7894.
789   10.1038/s41467-023-43666-5.
790 31. Huang, Y., Zhang, Y., and Ni, T. (2023). Towards in situ high-resolution imaging of viruses
791   and macromolecular complexes using cryo-electron tomography. J Struct Biol *215*, 108000.
792   10.1016/j.jsb.2023.108000.
793 32. Laurent, T., Kumar, P., Liese, S., Zare, F., Jonasson, M., Carlson, A., and Carlson, L.A. (2022).
794   Architecture of the chikungunya virus replication organelle. eLife *11*. 10.7554/eLife.83042.
795 33. Barad, B.A., Medina, M., Fuentes, D., Wiseman, R.L., and Grotjahn, D.A. (2023).
796   Quantifying organellar ultrastructure in cryo-electron tomography using a surface
797   morphometrics pipeline. The Journal of cell biology *222*. 10.1083/jcb.202204093.
798 34. Alimohamadi, H., and Rangamani, P. (2018). Modeling Membrane Curvature Generation due
799   to Membrane(-)Protein Interactions. Biomolecules *8*. 10.3390/biom8040120.
800 35. Helfrich, W. (1973). Elastic properties of lipid bilayers: theory and possible experiments. Z
801   Naturforsch C *28*, 693-703.
802 36. Rosendal, E., Bisikalo, K., Willekens, S.M.A., Lindgren, M., Holoubek, J., Svoboda, P.,
803   Lappalainen, A., Könighofer, E., Mirgorodskaya, E., Nordén, R., et al. (2024). The influence
804   of the pre-membrane and envelope proteins on structure, pathogenicity and tropism of tick-
805   borne encephalitis virus. bioRxiv, 2024.2010.2016.618642. 10.1101/2024.10.16.618642.

37. Keelapang, P., Sriburi, R., Supasa, S., Panyadee, N., Songjaeng, A., Jairungsri, A., Puttikhunt, C., Kasinrerk, W., Malasit, P., and Sittisombut, N. (2004). Alterations of pr-M cleavage and virus export in pr-M junction chimeric dengue viruses. J Virol *78*, 2367-2381. 10.1128/jvi.78.5.2367-2381.2004.

38. Garten, W. (2018). Characterization of Proprotein Convertases and Their Involvement in Virus Propagation. In Activation of Viruses by Host Proteases, E. Böttcher-Friebertshäuser, W. Garten, and H.D. Klenk, eds. (Springer Nature). 10.1007/978-3-319-75474-1_9.

39. Chotiwan, N., Rosendal, E., Willekens, S.M.A., Schexnaydre, E., Nilsson, E., Lindqvist, R., Hahn, M., Mihai, I.S., Morini, F., Zhang, J., et al. (2023). Type I interferon shapes brain distribution and tropism of tick-borne flavivirus. Nature communications *14*, 2007. 10.1038/s41467-023-37698-0.

40. Ahola, T. (2019). New Phylogenetic Grouping of Positive-Sense RNA Viruses Is Concordant with Replication Complex Morphology. mBio *10*. 10.1128/mBio.01402-19.

41. Akey, D.L., Brown, W.C., Dutta, S., Konwerski, J., Jose, J., Jurkiw, T.J., DelProposto, J., Ogata, C.M., Skiniotis, G., Kuhn, R.J., and Smith, J.L. (2014). Flavivirus NS1 structures reveal surfaces for associations with membranes and the immune system. Science (New York, N.Y *343*, 881-885. 10.1126/science.1247749.

42. Ci, Y., Liu, Z.Y., Zhang, N.N., Niu, Y., Yang, Y., Xu, C., Yang, W., Qin, C.F., and Shi, L. (2020). Zika NS1-induced ER remodeling is essential for viral replication. The Journal of cell biology *219*. 10.1083/jcb.201903062.

43. Huang, Y., Wang, T., Zhong, L., Zhang, W., Zhang, Y., Yu, X., Yuan, S., and Ni, T. (2024). Molecular architecture of coronavirus double-membrane vesicle pore complex. Nature *633*, 224-231. 10.1038/s41586-024-07817-y.

44. Wolff, G., Limpens, R., Zevenhoven-Dobbe, J.C., Laugks, U., Zheng, S., de Jong, A.W.M., Koning, R.I., Agard, D.A., Grünewald, K., Koster, A.J., et al. (2020). A molecular pore spans the double membrane of the coronavirus replication organelle. Science (New York, N.Y *369*, 1395-1398. 10.1126/science.abd3629.

45. Unchwaniwala, N., Zhan, H., Pennington, J., Horswill, M., den Boon, J.A., and Ahlquist, P. (2020). Subdomain cryo-EM structure of nodaviral replication protein A crown complex provides mechanistic insights into RNA genome replication. Proceedings of the National Academy of Sciences of the United States of America *117*, 18680-18691. 10.1073/pnas.2006165117.

46. Ertel, K.J., Benefield, D., Castano-Diez, D., Pennington, J.G., Horswill, M., den Boon, J.A., Otegui, M.S., and Ahlquist, P. (2017). Cryo-electron tomography reveals novel features of a viral RNA replication compartment. eLife *6*. 10.7554/eLife.25940.

47. Tan, Y.B., Chmielewski, D., Law, M.C.Y., Zhang, K., He, Y., Chen, M., Jin, J., and Luo, D. (2022). Molecular architecture of the Chikungunya virus replication complex. Sci Adv *8*, eadd2536. 10.1126/sciadv.add2536.

48. Laurent, T., and Carlson, L.A. (2023). The organization of double-stranded RNA in the chikungunya virus replication organelle. PLoS Negl Trop Dis *17*, e0011404. 10.1371/journal.pntd.0011404.

49. Kumar, M., and Altan-Bonnet, N. (2021). Viral pores are everywhere. Mol Cell *81*, 2061-2063. 10.1016/j.molcel.2021.04.025.

50. de Beijer, N.L., Snijder, E.J., and Barcena, M. (2024). A Cool Look at Positive-Strand RNA Virus Replication Organelles: New Insights from Cryo-Electron Microscopy. Annu Rev Biochem *93*, 163-187. 10.1146/annurev-biochem-052521-115736.

51. Goethals, O., Kaptein, S.J.F., Kesteleyn, B., Bonfanti, J.F., Van Wesenbeeck, L., Bardiot, D., Verschoor, E.J., Verstrepen, B.E., Fagrouch, Z., Putnak, J.R., et al. (2023). Blocking NS3-NS4B interaction inhibits dengue virus in non-human primates. Nature *615*, 678-686. 10.1038/s41586-023-05790-6.

52. Kaptein, S.J.F., Goethals, O., Kiemel, D., Marchand, A., Kesteleyn, B., Bonfanti, J.F., Bardiot, D., Stoops, B., Jonckers, T.H.M., Dallmeier, K., et al. (2021). A pan-serotype dengue virus inhibitor targeting the NS3-NS4B interaction. Nature *598*, 504-509. 10.1038/s41586-021-03990-6.

53. Kiemel, D., Kroell, A.H., Denolly, S., Haselmann, U., Bonfanti, J.F., Andres, J.I., Ghosh, B., Geluykens, P., Kaptein, S.J.F., Wilken, L., et al. (2024). Pan-serotype dengue virus inhibitor JNJ-A07 targets NS4A-2K-NS4B interaction with NS2B/NS3 and blocks replication organelle formation. Nat Commun 15, 6080. 10.1038/s41467-024-50437-3.

54. Gilbert, M.A.G., Fatima, N., Jenkins, J., O'Sullivan, T.J., Schertel, A., Halfon, Y., Wilkinson, M., Morrema, T.H.J., Geibel, M., Read, R.J., et al. (2024). CryoET of beta-amyloid and tau within postmortem Alzheimer's disease brain. Nature 631, 913-919. 10.1038/s41586-024-07680-x.

55. Schiotz, O.H., Kaiser, C.J.O., Klumpe, S., Morado, D.R., Poege, M., Schneider, J., Beck, F., Klebl, D.P., Thompson, C., and Plitzko, J.M. (2024). Serial Lift-Out: sampling the molecular anatomy of whole organisms. Nat Methods 21, 1684-1692. 10.1038/s41592-023-02113-5.

56. Nguyen, H.T.D., Perone, G., Klena, N., Vazzana, R., Kaluthantrige Don, F., Silva, M., Sorrentino, S., Swuec, P., Leroux, F., Kalebic, N., et al. (2024). Serialized on-grid lift-in sectioning for tomography (SOLIST) enables a biopsy at the nanoscale. Nat Methods 21, 1693-1701. 10.1038/s41592-024-02384-6.

57. Mastronarde, D.N. (2005). Automated electron microscope tomography using robust prediction of specimen movements. J Struct Biol 152, 36-51. S1047-8477(05)00152-8 [pii]

10.1016/j.jsb.2005.07.007.

58. Dahmane, S., Kerviel, A., Morado, D.R., Shankar, K., Ahlman, B., Lazarou, M., Altan-Bonnet, N., and Carlson, L.A. (2022). Membrane-assisted assembly and selective secretory autophagy of enteroviruses. Nature communications 13, 5986. 10.1038/s41467-022-33483-7.

59. Zheng, S.Q., Palovcak, E., Armache, J.P., Verba, K.A., Cheng, Y., and Agard, D.A. (2017). MotionCor2: anisotropic correction of beam-induced motion for improved cryo-electron microscopy. Nat Methods 14, 331-332. 10.1038/nmeth.4193.

60. Kremer, J.R., Mastronarde, D.N., and McIntosh, J.R. (1996). Computer visualization of three-dimensional image data using IMOD. J. Struct. Biol. 116, 71-76.

61. Xiong, Q., Morphew, M.K., Schwartz, C.L., Hoenger, A.H., and Mastronarde, D.N. (2009). CTF determination and correction for low dose tomographic tilt series. J Struct Biol 168, 378-387. 10.1016/j.jsb.2009.08.016.

62. Rohou, A., and Grigorieff, N. (2015). CTFFIND4: Fast and accurate defocus estimation from electron micrographs. J Struct Biol 192, 216-221. 10.1016/j.jsb.2015.08.008.

63. Buchholz, T.O., Jordan, M., Pigino, G., and Jug, F. (2019). Cryo-CARE: Content-Aware Image Restoration for Cryo-Transmission Electron Microscopy Data. I S Biomed Imaging, 502-506. 10.1109/isbi.2019.8759519.

64. Liu, Y.T., Zhang, H., Wang, H., Tao, C.L., Bi, G.Q., and Zhou, Z.H. (2022). Isotropic reconstruction for electron tomography with deep learning. Nature communications 13, 6482. 10.1038/s41467-022-33957-8.

65. Lamm, L., Zufferey, S., Righetto, R.D., Wietrzynski, W., Yamauchi, K.A., Burt, A., Liu, Y., Zhang, H., Martinez-Sanchez, A., Ziegler, S., et al. (2024). MemBrain v2: an end-to-end tool for the analysis of membranes in cryo-electron tomography. biorxiv. 10.1101/2024.01.05.574336

66. Pettersen, E.F., Goddard, T.D., Huang, C.C., Couch, G.S., Greenblatt, D.M., Meng, E.C., and Ferrin, T.E. (2004). UCSF Chimera--a visualization system for exploratory research and analysis. Journal of computational chemistry 25, 1605-1612. 10.1002/jcc.20084.

67. Erickson, H.P. (2009). Size and shape of protein molecules at the nanometer level determined by sedimentation, gel filtration, and electron microscopy. Biol Proced Online 11, 32-51. 10.1007/s12575-009-9008-x.

68. Tegunov, D., and Cramer, P. (2019). Real-time cryo-electron microscopy data preprocessing with Warp. Nat Methods 16, 1146-1152. 10.1038/s41592-019-0580-y.

69. Castano-Diez, D., Kudryashev, M., Arheit, M., and Stahlberg, H. (2012). Dynamo: a flexible, user-friendly development tool for subtomogram averaging of cryo-EM data in high-performance computing environments. J Struct Biol 178, 139-151. 10.1016/j.jsb.2011.12.017.

70. Castano-Diez, D., Kudryashev, M., and Stahlberg, H. (2017). Dynamo Catalogue: Geometrical tools and data management for particle picking in subtomogram averaging of cryo-electron tomograms. J Struct Biol *197*, 135-144. 10.1016/j.jsb.2016.06.005.

71. Schindelin, J., Arganda-Carreras, I., Frise, E., Kaynig, V., Longair, M., Pietzsch, T., Preibisch, S., Rueden, C., Saalfeld, S., Schmid, B., et al. (2012). Fiji: an open-source platform for biological-image analysis. Nat Methods *9*, 676-682. 10.1038/nmeth.2019.

72. Kurhade, C., Zegenhagen, L., Weber, E., Nair, S., Michaelsen-Preusse, K., Spanier, J., Gekara, N.O., Kroger, A., and Overby, A.K. (2016). Type I Interferon response in olfactory bulb, the site of tick-borne flavivirus accumulation, is primarily regulated by IPS-1. J Neuroinflammation *13*, 22. 10.1186/s12974-016-0487-9.

73. Panayiotou, C., Lindqvist, R., Kurhade, C., Vonderstein, K., Pasto, J., Edlund, K., Upadhyay, A.S., and Overby, A.K. (2018). Viperin Restricts Zika Virus and Tick-Borne Encephalitis Virus Replication by Targeting NS3 for Proteasomal Degradation. J Virol *92*. 10.1128/JVI.02054-17.

74. Pulkkinen, L.I.A., Barrass, S.V., Domanska, A., Overby, A.K., Anastasina, M., and Butcher, S.J. (2022). Molecular Organisation of Tick-Borne Encephalitis Virus. Viruses *14*. 10.3390/v14040792.

75. Jaimes, J.A., Millet, J.K., Goldstein, M.E., Whittaker, G.R., and Straus, M.R. (2019). A Fluorogenic Peptide Cleavage Assay to Screen for Proteolytic Activity: Applications for coronavirus spike protein activation. J Vis Exp. 10.3791/58892.

76. Artificial Cerebrospinal Fluid (ACSF) (10x). (2017). Cold Spring Harb Protoc *2017*. 10.1101/pdb.rec094342.

77. Zhang, J., Zhang, D., Sun, L., Ji, G., Huang, X., Niu, T., Xu, J., Ma, C., Zhu, Y., Gao, N., et al. (2021). VHUT-cryo-FIB, a method to fabricate frozen hydrated lamellae from tissue specimens for in situ cryo-electron tomography. J Struct Biol *213*, 107763. 10.1016/j.jsb.2021.107763.

29